

Characterizing Lyman alpha emission from high-redshift galaxies

Samuel Gagnon-Hartman¹, Andrei Mesinger^{2,5,1}, Ivan Nikolić^{3,4}, Eleonora Parlanti¹, and Giacomo Venturi¹

¹ Scuola Normale Superiore di Pisa, Piazza dei Cavalieri 7, 56126 Pisa, Italy

² Department of Physics and Astronomy “Ettore Majorana”, University of Catania, Via Santa Sofia 64, 95123 Catania, Italy

³ Cosmic Dawn Center (DAWN)

⁴ Niels Bohr Institute, University of Copenhagen, Jagtvej 128, 2200 Copenhagen N, Denmark

⁵ Centro Nazionale “High Performance Computing, Big Data and Quantum Computing”, Via Magnanelli, 40033 Casalecchio di Reno, Italy

Received February 6, 2026; accepted February 6, 2026

ABSTRACT

The Lyman α (Ly α) line from high-redshift galaxies is a powerful probe of the Epoch of Reionization (EoR). Neutral hydrogen in the intergalactic medium (IGM) can significantly attenuate the emergent Ly α line, even in the damping wing of the cross-section. However, interpreting this damping wing imprint relies on our prior knowledge of the spectrum that escapes from the galaxy and its environs into the IGM. This emergent spectrum is highly sensitive to the composition and geometry of the interstellar and circumgalactic media, and so exhibits a large galaxy to galaxy scatter. Characterizing this scatter is further complicated by non-trivial selection effects introduced by observational surveys. Here we build a flexible, empirical model for the emergent Ly α spectra. Our model characterizes the emergent Ly α luminosity, the velocity offset of the Ly α line with respect to the systemic redshift, and the H α luminosity, with multivariate probability distributions conditioned on the UV magnitude. We constrain these distributions using $z \sim 5 - 6$ galaxy observations with VLT MUSE and JWST NIRCam, forward-modeling observational selection functions together with galaxy parameters. Our model results in Ly α equivalent width distributions that are a better match to (independent) Subaru observations than previous empirical models. The extended distributions of Ly α equivalent widths and velocity offsets we obtain could facilitate Ly α transmission during the early stages of the EoR. We also illustrate how our model can be used to identify GN-z11-like outliers, potentially originating from merging systems. We publish fitting functions and make our model publicly available.

Key words. epoch of reionization – high-z galaxies

1. Introduction

The first stars, black holes and galaxies formed sometime during the first billion years, starting the so-called Cosmic Dawn (CD). The radiation from these galaxies spread out, heating and ionizing the intergalactic medium (IGM), culminating in the last phase change of our Universe: the Epoch of Reionization (EoR). The details of this process, including when reionization happened and which objects drove it, remain uncertain (see reviews by, e.g., Mesinger 2016; Dayal & Ferrara 2018). While a definitive measurement of the timing and morphology of reionization will likely come from the redshifted 21-cm line of neutral hydrogen, making this observation is very technically challenging and it might be a long time until we have robust data.

Currently one of the most powerful techniques to study the EoR is through the observed Lyman- α (Ly α) spectra of galaxies (e.g., Dijkstra 2014; Hutter et al. 2017; Mason et al. 2018; Jung et al. 2020; Umeda et al. 2025). During the EoR there is sufficient neutral hydrogen (HI) in the IGM to significantly attenuate Ly α even via the damping wing of the cross section. The damping wing attenuation can extend redward of the line center, impacting spectral regions that might otherwise be unaffected by resonant Ly α scattering from HI in the vicinity of the galaxy (Dijkstra 2014; Mesinger et al. 2015; Gelli et al. 2025). Identifying the IGM damping wing imprint in the observed Ly α spectra of a galaxy would allow us to measure the average hydro-

gen neutral fraction in the IGM, \bar{x}_{HI} , and even the EoR morphology (given a sufficiently large sample of galaxies; e.g. Furlanetto et al. 2006; McQuinn et al. 2007; Mesinger & Furlanetto 2008; Stark et al. 2010; Sobacchi & Mesinger 2015; Mason et al. 2018; Jung et al. 2020; Bolan et al. 2022; Lu et al. 2024; Nikolić et al. 2024; Nakane et al. 2024; Umeda et al. 2025; Jones et al. 2025).

Unfortunately, measuring the IGM damping wing imprint from the observed spectra requires knowing the Ly α profile that emerges from the galaxy into the IGM. Ly α in galaxies is primarily sourced by recombinations in the ionized interstellar medium (ISM) surrounding type-O and B stars (Gnedin & Hui 1998; Greif et al. 2009; Raiter et al. 2010; Pawlik et al. 2011), although collisionally excited HI in the ISM and circumgalactic medium (CGM) can act as a secondary source (Haiman et al. 2000; Fardal et al. 2001). To be detected, the Ly α photons must escape from the galaxy in the direction of the observer. HI and dust in the ISM and CGM resonantly scatter and absorb Ly α photons. The geometry of the ISM and CGM varies from galaxy to galaxy, rendering the relationship between intrinsic Ly α photon production and the emergent Ly α spectrum nontrivial.

Various models have been proposed which connect galaxy properties to properties of the emergent Ly α spectrum. These include analytic models, which make simplifying assumptions about galaxy geometry and composition to predict the emergent spectrum, radiative transfer simulations through the ISM and CGM, which aim to capture the full complexity of Ly α propagation in realistic environments, and empirical models, which

* email:samuel.gagnonhartman@sns.it

draw scaling relations between galaxy and Ly α properties from observations.

The fully analytic solution of Neufeld (1990) provides a handy relationship between the velocity offset of the Ly α line and the HI column density of the system, but this only holds in the case of a static slab geometry with a singly-peaked Ly α source placed at its center. Works employing numerical radiative transfer have since explored other geometries, most famously the expanding spherical shell and its variants (Verhamme et al. 2012; Gronke et al. 2016; Nebrin et al. 2025; Smith et al. 2025). Others combine galaxy simulations with radiative transfer to produce Ly α spectra not reliant on simple geometries (Behrens et al. 2018, 2019; Byrohl & Gronke 2020; Smith et al. 2022). Recent work by Khoraminezhad et al. (2025) aimed to bridge the gap between analytic and empirical modeling by fitting a series of empirical scaling relations to the input of zELDA, a Ly α spectrum emulator trained on a database of expanding spherical shell model spectra (zELDA: Gurung-López et al. 2025). They tuned the parameters of their model to accurately reproduce the luminosity function and clustering of Ly α -emitting galaxies at $z \sim 2-3$. While such simulations provide qualitative insight into emergent spectra, the inherent assumptions about ISM/CGM geometries can result in non-physical best-fit parameters (e.g. Li & Gronke 2022; Gronke 2017; Vitte et al. 2025).

Due to these challenges, studies of the EoR typically rely on empirical scaling relations that were fitted to observed Ly α spectra unattenuated by the EoR (i.e. at $z \lesssim 6$). For example, Mason et al. (2018) (M18) proposed a simple model which characterizes the probability of Ly α emission, the mean Ly α equivalent width, and the mean velocity offset as functions of the UV continuum magnitude M_{UV} (see also Treu et al. 2012; Tang et al. 2024a). Recently, Prieto-Lyon et al. (2025) expanded on such a model using a larger $z \sim 5$ dataset, fitting the Ly α equivalent width PDF as a function of UV magnitude and slope (although they find no dependence on the later). Such empirical relations are proving to be invaluable in interpreting the ever-increasing sample of Lyman alpha galaxy spectra during the EoR (e.g., Saxena et al. 2023; Tang et al. 2023; Chen et al. 2024; Napolitano et al. 2024; Tang et al. 2024b; Umeda et al. 2024; Witstok et al. 2025).

However, empirical models also have shortcomings. In the absence of guiding physics, the functional forms and dependencies need to be either chosen a priori or motivated by the data (e.g. using Bayesian model selection, see review by Trotta 2008). Whatever the choice of functional model, there is no guarantee that it can be generalized to other datasets. This is especially true if the data used to fit the model had inhomogeneous or poorly-understood selection effects. Biased observational samples, as well as poorly-chosen functional models, can yield spurious correlations or hide true correlations (e.g., Di Cesare et al. 2025).

Here we build a flexible, data-driven empirical model for the emergent (i.e. leaving the ISM/CGM and entering the IGM) Lyman alpha profile. Our model characterizes the emergent Ly α luminosity, the velocity offset of the Ly α line with respect to the systemic redshift, and the H α luminosity, with probability distributions conditioned on the UV magnitude. We also forward model selection effects together with the model parameters. We calibrate our model on the recent homogeneous sample from Tang et al. (2024a), composed of objects detected in Ly α by VLT MUSE and in H α by JWST NIRCam (MUSE-Wide: Urutia et al. 2019; MUSE-Deep: Bacon et al. 2017, 2023; JWST FRESCO: Oesch et al. 2023). We demonstrate that our model can reproduce high- z Ly α statistics, such as the Ly α luminosity function and equivalent width distribution measured by Umeda et al. (2025), despite being calibrated on an independent dataset.

This paper is organized as follows. Section 2 details the impact of selection effects on inferred probability distributions, describes the Tang et al. (2024a) (T24) galaxy sample and its selection criteria, and then goes on to describe our model and its calibration. A summary of our model is included at the end of the section for ease of implementation. Section 3 lists the correlations found by our model, giving analytic scaling relations for the Ly α luminosity, velocity offset, H α luminosity, Ly α escape fraction, and Ly α equivalent width with M_{UV} . Section 4 compares these relations to those found by previous work, and explores some consequences of our model. Section 5 enumerates our main results. Throughout this work we adopt the cosmology of Planck Collaboration et al. (2020), where $H_0 = 67.66 \text{ km s}^{-1}$, $\Omega_m = 0.30966$, and $\Omega_b = 0.04897$.

2. Methods

In this section, we first demonstrate potential biases imposed on empirical relations by observational effects and discuss existing methods which partially account for them. Then we introduce the form of our model and discuss the measurements required to constrain its parameters. We follow this by detailing the T24 dataset and how it fulfills the requirements of our model. Finally, we provide the likelihood function used to fit our model to the T24 dataset. We also include numbered instructions for implementing our model with all optimal parameters under the “Quick implementation” subsection.

Throughout this section, we refer to the following galaxy properties: the emergent Ly α luminosity, $L_{\text{Ly}\alpha}$, the velocity offset of the Ly α line with respect to the systemic redshift, Δv , the H α luminosity, $L_{\text{H}\alpha}$, and the UV continuum magnitude, M_{UV} .

2.1. Observational effects

An ideal survey of all galaxy spectra in the Universe would provide a direct measurement of the joint probability distribution $P(L_{\text{Ly}\alpha}, \Delta v, L_{\text{H}\alpha}, M_{\text{UV}})$. However, real surveys include various selection effects. In the simplest case, selection amounts to placing a conditional such that only a subset of an intrinsic distribution is observed¹.

Defining the Ly α /nebular properties of interest as:

$$x_\alpha = \{\log_{10} L_{\text{Ly}\alpha}, \Delta v, \log_{10} L_{\text{H}\alpha}\} \quad (1)$$

we would like to know the underlying (i.e. “true”) distribution $P(x_\alpha, M_{\text{UV}})$. However, we can only observe the conditional distribution $P(x_\alpha, M_{\text{UV}}|\text{obs})$, where obs is the condition that an object with properties $\{x_\alpha, M_{\text{UV}}\}$ is observed. These are related by the following:

$$P(x_\alpha, M_{\text{UV}}) = P(x_\alpha, M_{\text{UV}}|\text{obs})P(\text{obs}), \quad (2)$$

demonstrating that a measurement of $P(x_\alpha, M_{\text{UV}})$ requires an estimate of $P(\text{obs})$.

Figure 1 illustrates the simple example of a set of galaxies with measured M_{UV} and Ly α equivalent widths $W_{\text{emerg}}^{\text{Ly}\alpha}$. Through-

¹ In the more generic case, observational effects may alter the observed data such that the observed distribution is a transformation of the intrinsic distribution (e.g., slit losses reducing line fluxes of more extended emission, c.f. Napolitano et al. 2025). Here we assume that the treatment of JWST slit losses in the T24 analysis was correct, and therefore assume the simple case throughout this work.

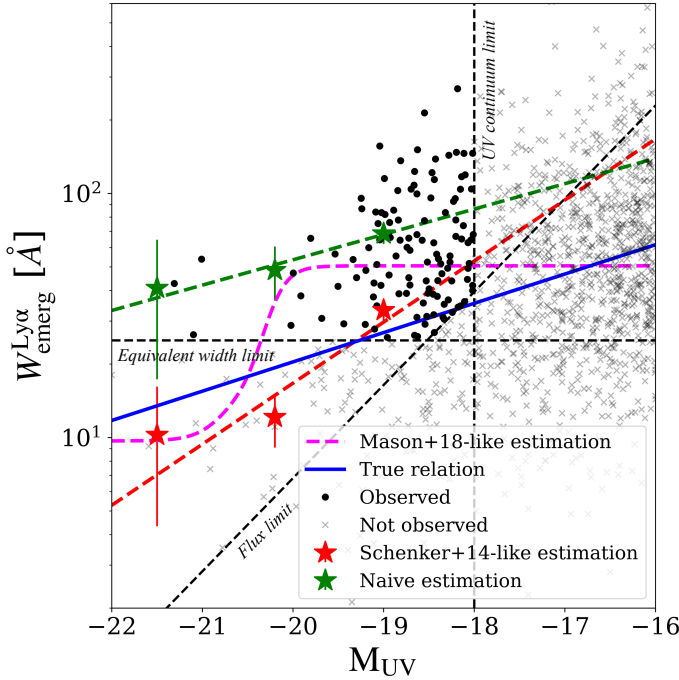


Fig. 1. Toy model illustrating the impact of observational selection bias on the inferred $\log_{10} W_{\text{emerg}}^{\text{Ly}\alpha} - M_{\text{UV}}$ relation. The black dashed lines show the completeness limits of a realistic Ly α survey (taken from De Barros et al. 2017). The blue curve traces the mean of a fiducial normal $\log_{10} W_{\text{emerg}}^{\text{Ly}\alpha} - M_{\text{UV}}$ relation. 1250 samples drawn from this distribution are shown with black dots (observed) and grey x's (non-observed). The green stars and line show the relation one obtains by linear regression to the observed samples. The red stars and line show the relation one obtains by linear regression on the observed samples, corrected for $W_{\text{emerg}}^{\text{Ly}\alpha}$ completeness using the method of Schenker et al. (2014). The pink dashed curve shows the mean relation one obtains by the fitting procedure of Mason et al. (2018).

out this work we define the emergent Ly α equivalent width as

$$W_{\text{emerg}}^{\text{Ly}\alpha}(L_{\text{Ly}\alpha}, M_{\text{UV}}) = \left(\frac{1215.67 \text{ \AA}}{2.47 \cdot 10^{15} \text{ Hz}} \right) 10^{-0.4(51.6 - M_{\text{UV}})} \times L_{\text{Ly}\alpha} \left(\frac{1215.67}{1500} \right)^{-\beta(M_{\text{UV}}) - 2}, \quad (3)$$

where we adopt

$$\beta(M_{\text{UV}}) = -0.2(M_{\text{UV}} + 19.5) - 2.05 \quad (4)$$

from the fit to *Hubble* Space Telescope UV slope measurements made by Bouwens et al. (2014). This set of galaxies is subjected to three selection criteria representative of those present in a typical Ly α survey: a minimum Ly α flux, minimum Ly α equivalent width, and a maximum M_{UV} ; in this example we adopt the criteria from De Barros et al. (2017): $W_{\text{emerg}}^{\text{Ly}\alpha} \geq 25 \text{ \AA}$, Ly α flux $> 2.2 \cdot 10^{-18} \text{ erg s}^{-1} \text{ cm}^{-2}$, and $M_{\text{UV}} \leq -18$. Each selection limit is shown with a black dashed line, and galaxies which meet all three criteria are shown in black dots while galaxies which do not are shown in grey x's. A fiducial true mean $W_{\text{emerg}}^{\text{Ly}\alpha} - M_{\text{UV}}$ relation is shown in a blue line, from which the log-normally distributed equivalent widths are drawn. If one were to naively treat the trend in the observed galaxies as representing the true trend, then the green line would be obtained. Clearly, an estimate of $P(\text{obs}|M_{\text{UV}})$ is required to correct this relation.

Most previous work on estimating mean $W_{\text{emerg}}^{\text{Ly}\alpha} - M_{\text{UV}}$ relations used spectroscopic follow-up of a photometric dataset complete down to some M_{UV} . In these cases, the galaxies with detected M_{UV} and non-detected Ly α can be used to estimate the $P(\text{obs}|M_{\text{UV}})$. One could estimate a simple step-function form for $P(\text{obs}|M_{\text{UV}})$ by splitting the data into M_{UV} bins and dividing the number of galaxies with observed Ly α emission by the total number of galaxies in the bin. M18 followed this approach in their empirical fit of the distribution of Ly α equivalent widths to a set of LBGs with VLT FORS2 spectra. In their analysis, they split their data into three M_{UV} bins, computed the mean equivalent width and observed fraction in each, and then fit each with a tanh function. In their model, the product of these functions may be taken as the mean $W_{\text{emerg}}^{\text{Ly}\alpha} - M_{\text{UV}}$ relation. Schenker et al. (2014) performed a similar exercise on a set of Lyman-break galaxies (LBGs) with MOSFIRE spectroscopic follow-up from the Keck telescope. However, instead of directly estimating $P(\text{obs}|M_{\text{UV}})$, Schenker et al. (2014) performed a linear regression on all galaxies, treating those with no detected Ly α emission as having an equivalent width of zero. In Figure 1, we show the fits one would obtain by following the approaches of Schenker et al. (2014) and M18 on our mock data. While these models provide a better approximation of $P(W_{\text{emerg}}^{\text{Ly}\alpha}|M_{\text{UV}})$ than the naive fit, they do not recover the true mean relation. Furthermore, they do not capture the intrinsic scatter around this mean relation.

In addition to observational selection effects, we assume that the infalling CGM attenuates all Lyman alpha flux blueward of the galaxy's circular velocity (e.g. Barkana & Loeb (2003)), computed as:

$$v_{\text{circ}} = [10GM_h H(z)]^{1/3}, \quad (5)$$

G is the constant of universal gravitation, M_h is the halo mass², and $H(z)$ is the Hubble constant at the redshift of the galaxy, z . We assume that only galaxies with $\Delta v \geq v_{\text{circ}}$ have observed Lyman alpha flux.

Summarizing observational effects which depend on survey properties as \mathcal{T} , we may say that the distribution of Ly α parameters measured in a real survey is $P(L_{\text{Ly}\alpha}, \Delta v, L_{\text{H}\alpha}, M_{\text{UV}}|\mathcal{T}, \Delta v > v_{\text{circ}})$. In what follows, we recover $P(L_{\text{Ly}\alpha}, \Delta v, L_{\text{H}\alpha}, M_{\text{UV}})$ by designing a model and calibration scheme which allow us to accurately estimate $P(\mathcal{T}, \Delta v > v_{\text{circ}})$.

2.2. Empirical model

The relationship between the spectral properties of interest, x_α (c.f. Eq. 1), and any other galaxy properties, x_{gal} , can generically be described by the joint probability distribution $P(x_\alpha, x_{\text{gal}})$. In the context of our model, we assume the only relevant functional dependence is the UV magnitude, $x_{\text{gal}} = \{M_{\text{UV}}\}$. We take advantage of the identity $P(x_\alpha, M_{\text{UV}}) = P(x_\alpha|M_{\text{UV}})P(M_{\text{UV}})$ and the fact that $P(M_{\text{UV}})$ is a known (observed) quantity, allowing us to solve only for the conditional distribution $P(x_\alpha|M_{\text{UV}})$. Note that fitting a conditional PDF is computationally easier and can be done with a smaller sample, compared to fitting a joint PDF, as discussed further below.

² Since our model does not include M_h , we adopt the broken linear relation of Mason et al. (2015) to relate M_h to M_{UV} : $\log_{10} M_h [\text{M}_\odot] = \gamma(M_{\text{UV}} + 20.0 + 0.26z) + 11.75$, where $\gamma = -0.3$ for $M_{\text{UV}} \geq -20.0 - 0.26z$, and $\gamma = -0.7$ otherwise.

We fix $P(M_{\text{UV}})$ to the Schechter fit of the $z \sim 5$ *Hubble* UV luminosity function (UVLF) of Bouwens et al. (2021):

$$P(M_{\text{UV}}) \propto (0.4 \ln 10) \cdot 0.79 \cdot \left(10^{-0.4(M_{\text{UV}}+21.1)}\right)^{-0.74} \times \exp\left\{-10^{-0.4(M_{\text{UV}}+21.1)}\right\}. \quad (6)$$

Importantly, the parameters in x_α are not independently distributed; for example, the $\text{H}\alpha$ luminosity of a galaxy typically increases with its $\text{Ly}\alpha$ luminosity since both trace the star formation rate (e.g., Kennicutt 1998). To account for these covariances, we model the conditional distribution $P(x_\alpha|M_{\text{UV}})$ as a multivariate Gaussian³ whose mean is a function of M_{UV} , i.e.,

$$P(x_\alpha|M_{\text{UV}}) \propto \exp\left\{-\frac{1}{2}(x_\alpha - \mu(M_{\text{UV}}))^T \Sigma^{-1} (x_\alpha - \mu(M_{\text{UV}}))\right\}, \quad (7)$$

where the means scale linearly with M_{UV} such that $\mu(M_{\text{UV}}) = m \cdot M_{\text{UV}} + b$, where m and b are 3-dimensional vectors, and Σ is the symmetric 9-dimensional covariance matrix of the distribution.

2.3. Observational sample

T24 presents a set of galaxies in the GOODS-S field at $z \sim 5$ with detected $\text{Ly}\alpha$ and $\text{H}\alpha$ lines. These galaxies were observed with both VLT MUSE and *JWST* NIRCam, of which 24 lie in the MUSE-Wide field and 36 lie in the MUSE-Deep field (MUSE-Wide: Urrutia et al. 2019; MUSE-Deep: Bacon et al. 2017, 2023; *JWST* FRESCO: Oesch et al. 2023). The T24 sample includes only galaxies with $M_{\text{UV}} \gtrsim -17.75$ and with line fluxes exceeding the 5σ flux limit of each survey. T24 reports the $\text{Ly}\alpha$ luminosity, $\text{H}\alpha$ luminosity, velocity offset of the $\text{Ly}\alpha$ line, and UV continuum magnitude of each galaxy in their sample. Table 1 lists the 5σ limiting flux for each survey. We divide the T24 sample into two datasets:

- T24-Deep. All galaxies detected in $\text{Ly}\alpha$ by MUSE-Deep in the MOSAIC, UDF-10, and MXDF fields. Each galaxy also has an $\text{H}\alpha$ detection from *JWST* FRESCO.
- T24-Wide. All galaxies detected in $\text{Ly}\alpha$ by MUSE-Wide, excluding those also detected by MUSE-Deep. Each galaxy also has an $\text{H}\alpha$ detection from *JWST* FRESCO.

The observational limits of these datasets, summarized in Table 2, were fit during the calibration of our model, where the effective equivalent width limits are imposed by the fixed M_{UV} limit.

The T24 galaxy sample offers two distinct advantages: (i) the galaxies lie in a field with overlapping MUSE and *JWST* grism observations, providing measurements of both the $\text{Ly}\alpha$ line and $\text{H}\alpha$ line in all reported sources, and (ii) the exposure times are nearly uniform across the observing area, allowing us to characterize the completeness in terms of thresholds in $\text{Ly}\alpha$, $\text{H}\alpha$, and continuum emission. The former gives us a handle on the escape fraction of $\text{Ly}\alpha$ from galaxies, and the latter provides well-defined priors for the selection effects.

³ Because a galaxy's luminosity can be expressed as a product of only weakly correlated terms (e.g. number of young stars, stellar SEDs, ISM/CGM opacity along a sightline), the central limit theorem could be used to roughly motivate log-normal luminosity distributions for a given galaxy population (e.g. at a fixed UV magnitude).

2.4. Model calibration

In this section, we describe how we fit the free parameters of the model described in Section 2.2 to the T24 datasets. In what follows, x_α refers to a spectral parameter vector sampled from our model (c.f. Eq. 1), while $\{x_\alpha^{\text{T24,Wide}}, x_\alpha^{\text{T24,Deep}}\}$ refer to the parameters quoted in the T24-Wide and T24-Deep datasets, respectively. We solve for values of m , b , and Σ which satisfy the condition:

$$P(x_\alpha|M_{\text{UV}})P(M_{\text{UV}}) = P(x_\alpha|M_{\text{UV}}, \mathcal{T}_{\text{T24},i})P(\mathcal{T}_{\text{T24},i}|M_{\text{UV}})P(M_{\text{UV}}), \quad (8)$$

where the indices i correspond to the T24-Wide and -Deep datasets and the observational selection functions, $\mathcal{T}_{\text{T24},i}$, are sigmoid functions ranging from 0 to 1 with midpoints parameterized by their equivalent width completeness limits W_{Wide} and W_{Deep} , and their flux limits f_{Wide} , f_{Deep} , and f_{JWST} . $P(x_\alpha|M_{\text{UV}}, \mathcal{T}_{\text{T24},i})$ and $P(M_{\text{UV}})$ correspond to the smoothed distribution of T24 data and the *Hubble* UVLF, respectively, so they remain fixed during our calibration. Meanwhile, the parameters of the *intrinsic* distribution of $\text{Ly}\alpha$ properties (i.e. before applying selection effects), $P(x_\alpha|M_{\text{UV}})$, and those of the observational selection functions, $P(\mathcal{T}_{\text{T24},i}|M_{\text{UV}})$, are free parameters fit during calibration. A schematic summarizing our approach is shown in Figure 2.

Our model assumes that $P(x_\alpha|M_{\text{UV}})$ is a multivariate Gaussian whose mean is a linear function of M_{UV} . Therefore we have 15 free parameters of the model (m and b are each 3-dimensional, while Σ is 9-dimensional; c.f. Eq. 7), in addition to 5 nuisance parameters related to selection (c.f. Table 2 and Appendix C). Since performing regression in 20 dimensions using only the T24 dataset would be challenging, we reduce the dimensionality of the problem by splitting it in two maximum likelihood estimation (MLE) steps:

1. In the first step, we solve for the covariance matrix of the *intrinsic* distribution of $\text{Ly}\alpha$ parameters, which we treat as a weighted sum of four basis matrices: a 4-dimensional MLE.
2. In the second step, we solve for the 6 mean parameters and 3 variance parameters in the orthonormal basis, plus the 5 nuisance parameters: a 14-dimensional MLE.

In both steps, we transformed our data to a space with zero mean and unit variance, defining $x_\alpha = \sigma_{\text{Ly}\alpha} x_{\alpha,0} + \mu_{\text{Ly}\alpha}$, where $x_{\alpha,0}$ is the unit variance zero mean parameter space. We used the mean and standard deviation from the T24-Deep dataset for this transformation since it contains more samples and should better reflect the tails of the distribution.

For the first step, we define the transformation A and eigenvector u , where $x_{\alpha,0} = Au$. We solve for A by minimizing the objective function

$$\text{obj} = \sum_i \left(u - x_{\alpha,i}^{\text{T24,Deep}}\right)^T \text{Cov}^{-1}(u) \left(u - x_{\alpha,i}^{\text{T24,Deep}}\right), \quad (9)$$

describing the similarity of the samples $u \sim P(x_\alpha|\mathcal{T}_{\text{T24,Deep}})$ to the data $x_\alpha^{\text{T24,Deep}}$, using differential evolution (Storn & Price

⁴ We expect the correlations in the MUSE-Deep sample to at least partially reflect the intrinsic correlations between $\text{Ly}\alpha$ parameters. The MUSE-Wide selection cuts out far more objects, meaning that the correlations in the surviving sample of objects mostly reflects the correlations imposed by the selection itself.

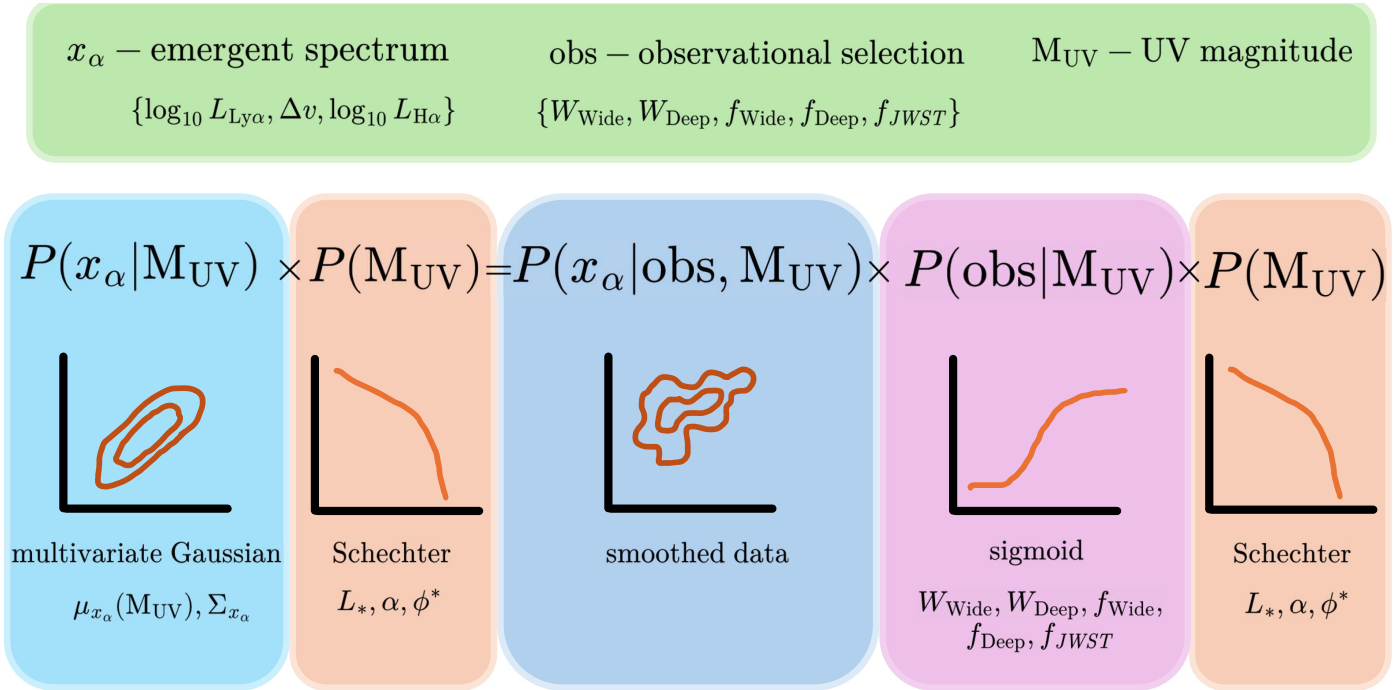


Fig. 2. Schematic overview of our model. We model $P(x_\alpha|M_{\text{UV}})$ as a multivariate Gaussian distribution conditioned on M_{UV} , and fit the parameters of this distribution, along with the parameters related to selection, labeled obs , to the measured distribution of the data $P(x_\alpha|\text{obs}, M_{\text{UV}})$. We bin the data in M_{UV} to take advantage of the Schechter fit to the measured UV luminosity function of Bouwens et al. (2021). All observational selection functions are modeled as sigmoids, varying from 0 to 1, whose inflection points are free parameters.

Table 1. Survey limiting fluxes reported by Tang et al. (2024a). Each flux corresponds to the 5σ detection limit of the relevant line in each survey.

Survey	Target line	Limiting flux [$\text{erg s}^{-1} \text{cm}^{-2}$]
MUSE-Wide	$\text{Ly}\alpha$	$2 \cdot 10^{-18}$
MUSE-Deep (MOSAIC)	$\text{Ly}\alpha$	$5 \cdot 10^{-19}$
MUSE-Deep (UDF-10)	$\text{Ly}\alpha$	$2.5 \cdot 10^{-19}$
MUSE-Deep (MXDF)	$\text{Ly}\alpha$	$1 \cdot 10^{-19}$
<i>JWST</i> FRESCO	$\text{H}\alpha$	$2 \cdot 10^{-18}$

Table 2. Galaxy datasets with relevant limiting fluxes, UV continuum magnitudes, and $\text{Ly}\alpha$ equivalent widths.

Dataset	$W_{\text{emerg,lim}}^{\text{Ly}\alpha}$ [\text{\AA}]	$f_{\text{Ly}\alpha,\text{lim}}$ [$\text{erg s}^{-1} \text{cm}^{-2}$]	$f_{\text{H}\alpha,\text{lim}}$ [$\text{erg s}^{-1} \text{cm}^{-2}$]	$M_{\text{UV,lim}}$
T24-Wide	116	$1.8 \cdot 10^{-17}$	$1.2 \cdot 10^{-18}$	-17.75
T24-Deep	24	$2.7 \cdot 10^{-18}$	$1.2 \cdot 10^{-18}$	-17.75

1997). We define A as a sum of basis transformations, $A = c_1 \mathcal{I} + c_2 S_1 + c_3 S_2 + c_4 S_3$, where \mathcal{I} is the identity matrix, and S_i are the first, second, and third transformation matrices of the $\text{SO}(3)$ special orthogonal Lie group (listed in Appendix A), and c_i are the free parameters optimized by differential evolution.

In the second step we solve for the remaining free parameters of the multivariate Gaussian and the observational selection functions by matching both sides of Eq. 8. Our likelihood function, again minimized by differential evolution (Storn & Price 1997), is a Gaussian distance computed on the following quantities: the observed fraction f_{obs} , the emergent $\text{Ly}\alpha$ equivalent width $W_{\text{emerg}}^{\text{Ly}\alpha}$, the velocity offset Δv , and the $\text{Ly}\alpha$ escape fraction $f_{\text{esc}}^{\text{Ly}\alpha}$. The functional form of this likelihood is given in Appendix B. We define $f_{\text{obs}}(M_{\text{UV}})$ as the fraction of total galaxies at a given M_{UV} in a given field of view which would be included

in a dataset given its observational selection function:

$$f_{\text{obs}}(M_{\text{UV}}|\mathcal{T}) = \frac{P(\text{obs}|\mathcal{T}, M_{\text{UV}})}{P(M_{\text{UV}})}. \quad (10)$$

In computing the escape fraction of $\text{Ly}\alpha$, we assume that the intrinsic $\text{Ly}\alpha$ luminosity arises from case A recombination (Osterbrock 1989; Hayes et al. 2010; Matthee et al. 2016; Yang et al. 2017; Chen et al. 2024; Saxena et al. 2024), where $L_{\text{Ly}\alpha}^{\text{intr}} = 11.4 L_{\text{H}\alpha}$. Therefore,

$$f_{\text{esc}}^{\text{Ly}\alpha}(L_{\text{Ly}\alpha}, L_{\text{H}\alpha}) = \frac{L_{\text{Ly}\alpha}}{11.4 L_{\text{H}\alpha}}. \quad (11)$$

Figure 3 shows the fraction of galaxies in the observation field observed in both $\text{Ly}\alpha$ and $\text{H}\alpha$ as a function of M_{UV} for both the T24-Deep and T24-Wide samples, as well as those of our calibrated model. Our model correctly captures both the trend

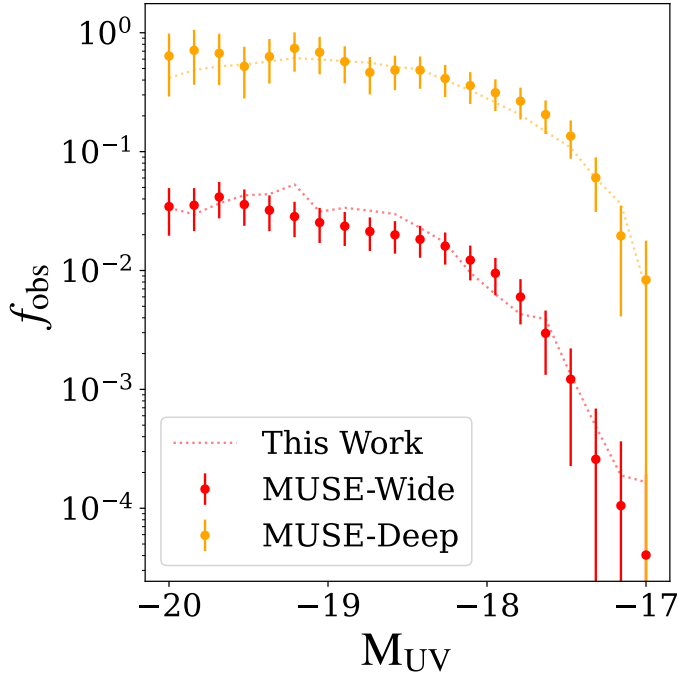


Fig. 3. The fraction of galaxies in the observation field observed in both Ly α and H α as a function of M_{UV}, shown in orange for T24-Deep and red for T24-Wide. Points with error bars are estimated from the T24 data, while dotted lines show the same statistic computed from a realization of our model.

of decreasing f_{obs} with decreasing UV luminosity as well as the global difference in f_{obs} between the deep and wide fields. The observed fraction constrains the distance between the mean of $P(x_\alpha)$ and the observed mean, $P(x_\alpha|\mathcal{T})$. Measuring the observed mean for two different observational selection functions allows the model to estimate the variance in $P(L_{\text{Ly}\alpha}, L_{\text{H}\alpha}|\text{M}_{\text{UV}})$.

2.5. Quick implementation

We obtain the following procedure for sampling galaxy Ly α properties:

1. Draw $\text{M}_{\text{UV}} \sim P(\text{M}_{\text{UV}})$
2. Draw $u \sim P(u|\text{M}_{\text{UV}}) = \mathcal{N}(\mu(\text{M}_{\text{UV}}), \sigma)$
3. Transform $x_{\alpha,0} = Au$
4. Transform $x_\alpha = \sigma_{\text{Ly}\alpha} x_{\alpha,0} + \mu_{\text{Ly}\alpha}$.

Here, $P(\text{M}_{\text{UV}})$ is the UVLF in Eq. 6, the eigenvectors u follow the distributions

$$\begin{aligned} u_1 &\sim \mathcal{N}(8.7 \cdot 10^{-2} \text{M}_{18.5} - 0.51, 0.7) \\ u_2 &\sim \mathcal{N}(-0.57 \text{M}_{18.5} - 0.85, 0.49) \\ u_3 &\sim \mathcal{N}(-0.38 \text{M}_{18.5} - 0.31, 0.26), \end{aligned} \quad (12)$$

where $\text{M}_{18.5} \equiv \text{M}_{\text{UV}} + 18.5$, the change of basis transformation is

$$A = \begin{bmatrix} 1 & 1 & 1/3 \\ -1 & 1 & -1 \\ -1/3 & 1 & 1 \end{bmatrix}, \quad (13)$$

and the mean and standard deviation of the data distribution are $\mu_{\text{Ly}\alpha} = \{42.47, 200.18, 42.03\}$ and $\sigma_{\text{Ly}\alpha} = \{0.42, 99.7, 0.39\}$,

respectively. Appendix C includes a table of all model parameters. We also include a more concise representation of the model as a multivariate normal distribution in Appendix D. The code used for calibration and sampling from our model is publicly available⁵.

3. Results

In this section, we first illustrate the parameter covariances in our model and then show that our model can reproduce the distribution of the T24 data. We list closed functional forms for the marginal distributions of each Ly α parameter conditioned on M_{UV}. We also provide functional forms for the marginal distributions of $W_{\text{Ly}\alpha}^{\text{emerg}}(\text{M}_{\text{UV}})$ and $f_{\text{esc}}^{\text{Ly}\alpha}(\text{M}_{\text{UV}})$.

Figure 4 illustrates the scalings between Ly α parameters in our model with various 2D slices of our full parameter distribution. In each slice, we sample $\text{M}_{\text{UV}} \sim \text{Unif}[-24, -16]$ for clarity. The bottom row shows how our Ly α parameters scale with M_{UV}. Each marginal distribution, $P(x_\alpha|\text{M}_{\text{UV}})$, is normally-distributed with a mean that varies linearly with UV magnitude and a constant standard deviation:

$$\log_{10}\left(\frac{L_{\text{Ly}\alpha}(\text{M}_{\text{UV}})}{\text{erg s}^{-1}}\right) = -0.28(\text{M}_{\text{UV}} + 18.5) + 41.86 \pm 0.36, \quad (14)$$

$$\Delta v(\text{M}_{\text{UV}}) = -27.92(\text{M}_{\text{UV}} + 18.5) + 197.19 \pm 89.17 \text{ km s}^{-1}, \quad (15)$$

$$\log_{10}\left(\frac{L_{\text{H}\alpha}(\text{M}_{\text{UV}})}{\text{erg s}^{-1}}\right) = -0.38(\text{M}_{\text{UV}} + 18.5) + 41.64 \pm 0.24, \quad (16)$$

each written as mean \pm standard deviation. The mean emergent Ly α and H α luminosities increase with increasing UV luminosity, as expected since all scale with the star formation rate of a galaxy. The velocity offset of the emergent Lyman alpha line with respect to its systemic redshift, Δv , also increases with UV luminosity, albeit with high scatter.

Now we investigate the joint distribution $P(x_{\text{Ly}\alpha}, \text{M}_{\text{UV}})$ produced by our model, which we produce by repeating the above exercise while using the UV luminosity function (Eq. 6) for $P(\text{M}_{\text{UV}})$. Figure 5 shows the joint distributions of $W_{\text{emerg}}^{\text{Ly}\alpha}$, Δv , and $f_{\text{esc}}^{\text{Ly}\alpha}$ with M_{UV} measured by Tang et al. (2024a) and predicted by our model. The bottom row shows the intrinsic distribution of parameters, with no selection effects applied. The top and middle rows respectively include the selection effects of T24-Deep and T24-Wide (see Table 2 for selection criteria). Our model fits both the T24-Wide and T24-Deep datasets very well.

Combining Eq.s 14-16 with Eq.s 3 and 11 yields $f_{\text{esc}}^{\text{Ly}\alpha}(\text{M}_{\text{UV}})$ and $W_{\text{emerg}}^{\text{Ly}\alpha}(\text{M}_{\text{UV}})$:

$$\log_{10} f_{\text{esc}}^{\text{Ly}\alpha}(\text{M}_{\text{UV}}) = 0.12(\text{M}_{\text{UV}} + 18.5) + 0.28 \pm 0.46 - \log_{10} \alpha_{\text{rec}}, \quad (17)$$

where α_{rec} is the ratio between the intrinsic luminosity of Ly α and that of H α ($\alpha_{\text{rec}} = 11.4$ for case A recombination and $\alpha_{\text{rec}} = 8.2$ for case B; Baker & Menzel (1938); Osterbrock (1989); Dijkstra (2014)), and

$$\log_{10} W_{\text{emerg}}^{\text{Ly}\alpha}(\text{M}_{\text{UV}}) [\text{\AA}] = 0.12(\text{M}_{\text{UV}} + 18.5) + 1.49 \pm 0.36. \quad (18)$$

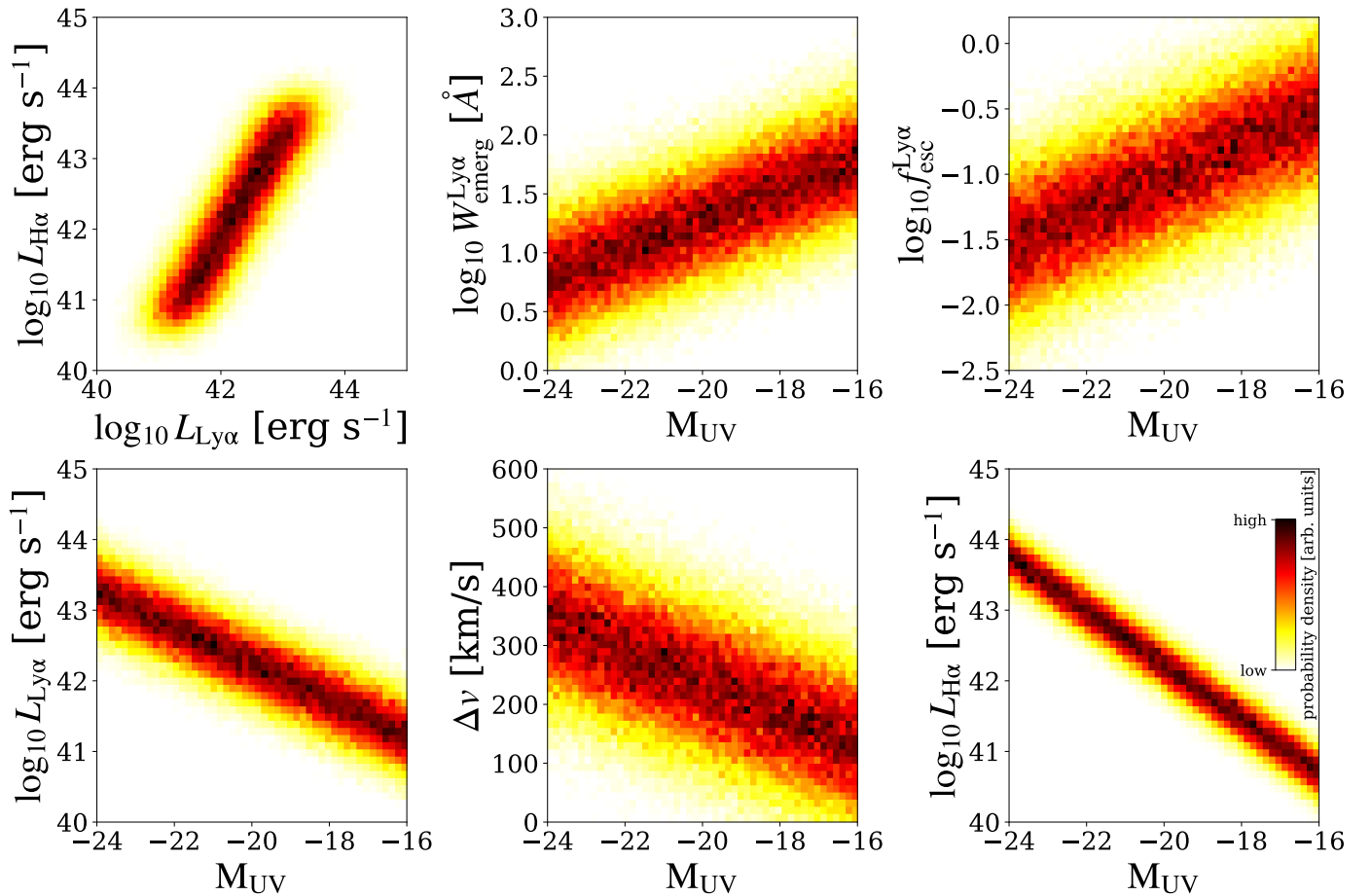


Fig. 4. Scalings between select Ly α parameters in our model. For better visualization of the trends at the rare/bright end, this figure was generated by uniformly sampling M_{UV} over the range shown. The Ly α luminosity, H α luminosity, and velocity offset of the Ly α line all increase with increasing UV continuum luminosity (bottom row) whereas the Ly α emergent equivalent width and escape fraction increase for decreasing UV continuum luminosity (top row).

4. Discussion

Here we compare our derived Ly α properties to previous works and discuss some implied trends.

4.1. Comparison with previous work

Before examining physical implications and application of our model, we compare the statistics predicted by our model with those reported by Mason et al. (2018), Prieto-Lyon et al. (2025), Tang et al. (2024a), and Umeda et al. (2025).⁶

Umeda et al. (2025) reported a huge suite of $\sim 20,000$ LAEs detected through Subaru photometry at $z \in [2.2, 7.3]$ and computed several summary statistics of their LAE population, including the equivalent width distribution (EW PDF). Figures 6 and 7 show a double power law fit to the EW PDF and the Ly α luminosity function (LAE LF) reported by Umeda et al. (2025) at $z \sim 5$, together with those produced by realizations of our model and the models of Mason et al. (2018) and Prieto-Lyon et al. (2025). We also show the EW PDF estimated by Tang et al. (2024a). These EW PDFs are marginalized over $M_{\text{UV}} \leq -18$.

Tang et al. (2024a) estimated the EW PDF by fitting log-normal distributions to subsets of their data. We produced the blue curve shown in Figure 6 by taking a weighted average of their log-normal fits to Lyman-break-selected galaxies in the T24 data centered at $M_{\text{UV}} = -18.5$ and $M_{\text{UV}} = -19.5$, where we set the weights equal to the value of the UVLF at those magnitudes. The T24 model is fit to primarily low- $W_{\text{emerg}}^{\text{Ly}\alpha}$ objects using a log-normal distribution, so its accuracy decreases at the high $W_{\text{emerg}}^{\text{Ly}\alpha}$ relevant to the LAELF in Figure 6.

Mason et al. (2018) (M18) introduced an empirical model of Ly α emission which has since been applied in several works (e.g., Umeda et al. 2025; Lu et al. 2025; Gagnon-Hartman et al. 2025; Nikolić et al. 2025) and has been shown to reproduce the LAE LF at $z \sim 2 - 6$ (Morales et al. 2021). The M18 model assumes that all galaxies have a probability $A(M_{\text{UV}})$ of emitting in Ly α an equivalent width drawn from an exponential distribution of mean $W_c(M_{\text{UV}})$ (Dijkstra & Wyithe 2012). The line profile is assumed to be a Gaussian whose FWHM equals its Δv , and they assume that a neutral CGM absorbs all Ly α emission with $\Delta v < v_{\text{circ}}$ (see Eq. 5). M18 modeled $A(M_{\text{UV}})$ and $W_c(M_{\text{UV}})$ as tanh functions fit to a sample of $z \sim 6$ LAEs detected in the VANDELLS ESO spectroscopic survey, a Large Program of the VLT (Pentericci et al. 2018). The procedure used by M18 to recover the $W_{\text{emerg}}^{\text{Ly}\alpha} - M_{\text{UV}}$ relation is prone to including unquantified bias (c.f. Section 2.1 and Figure 1). We provide recalibrated versions

⁵ https://github.com/samgagnon/empirical_lya

⁶ We opt not to compare our model with that of Khoraminezhad et al. (2025) since theirs is calibrated to objects at $z \sim 2 - 3$, while ours focuses on $z \sim 5$.

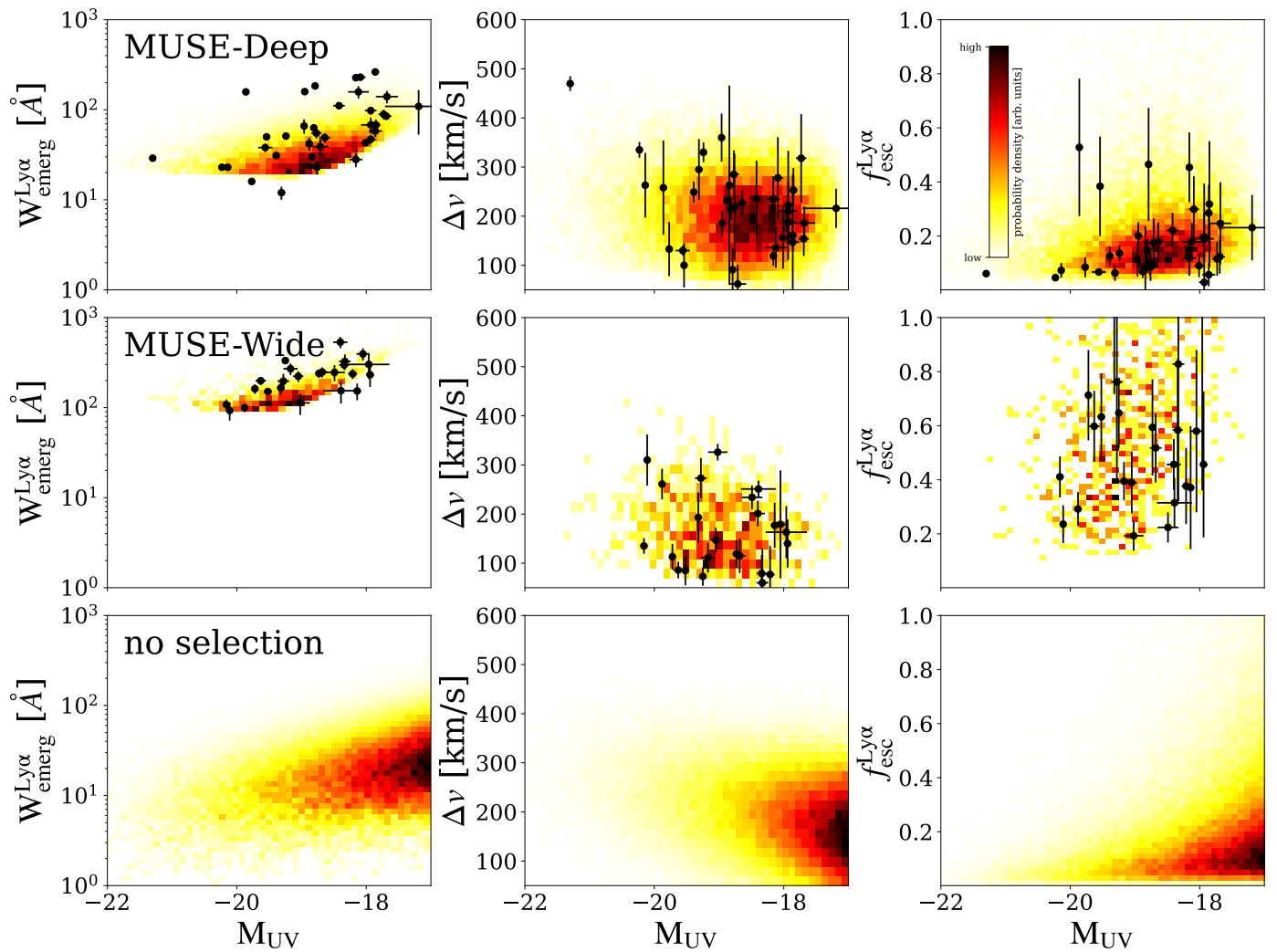


Fig. 5. The distribution of Ly α properties predicted by our model (red-orange probability density function) and measured by Tang et al. (2024a) (black points). The top row applies the flux completeness limits of MUSE-Deep and the *JWST* FRESCO survey, the second row applies that of MUSE-Wide and the *JWST* FRESCO survey, and the third row applies no selection effects. The PDF in each panel is normalized independently for visibility.

of their functions which better match the measured EW PDF of Umeda et al. 2025 in Appendix F.

When compared to the measured EW PDF from Subaru, M18 tends to overproduce low- $W_{\text{emerg}}^{\text{Ly}\alpha}$ and underproduce high- $W_{\text{emerg}}^{\text{Ly}\alpha}$ LAEs, especially beyond $W_{\text{emerg}}^{\text{Ly}\alpha} \sim 300$. In both regimes our model comes closer to the measured EW PDF. We attribute the accuracy of our model to its accurate determination of the variance in the $M_{\text{UV}} - W_{\text{emerg}}^{\text{Ly}\alpha}$ relation (e.g., Dijkstra & Wyithe 2012). This is made possible by: (i) having more flexible conditional PDFs; and (ii) the inclusion of both a deep and wide field in our calibration dataset. We present further evidence of the usefulness of (ii) in Appendix E. We note that our model diverges from the measured EW PDF at $W_{\text{Ly}\alpha}^{\text{emerg}} \approx 200$ Å: this is expected since Umeda et al. (2025) reports a double power law fit to the measured EW PDF, and we expect the transition between these domains to be smooth, likely closer to our model than the yellow curve. We stress that our model was exclusively calibrated on the T24 data, and therefore its ability to reproduce the EW PDF and LAE LF of Umeda et al. (2025) indicate the general applicability of the scaling relations and covariances reported in our study.

Prieto-Lyon et al. (2025) explored the dependence of $W_{\text{emerg}}^{\text{Ly}\alpha}$, $f_{\text{esc}}^{\text{Ly}\alpha}$, and Δv on the UV magnitude and slope. They used NIR-CAM/grism spectra of galaxies in the GOODS-N field complete in M_{UV} down to -19 (Eisenstein et al. 2023). The scalings found for $W_{\text{emerg}}^{\text{Ly}\alpha}$ and trend for Δv qualitatively agree with our own, as does their reported lack of a significant correlation between $f_{\text{esc}}^{\text{Ly}\alpha}$ and M_{UV} , since this correlation is low for the UV-bright objects in their dataset. While the EW PDF of their model is consistent with that of M18, we find that their LAE LF underproduces Ly α -bright objects relative to the Umeda et al. (2025) measurement (c.f. Figs. 6-7).

4.2. GS-z13 – is it surprising to detect Ly α at $z \sim 13$?

Witstok et al. (2025) presented GS-z13, a spectroscopically-confirmed Ly α -emitting galaxy at $z \sim 13$, whose relevant properties we list in Table 3. The detection of Ly α emission in the early stages of the EoR (e.g. Qin et al. 2024) suggests either that GS-z13 is emitting significant Ly α at a high velocity offset relative to the neutral gas surrounding it (i.e. with a large $L_{\text{Ly}\alpha}$ and

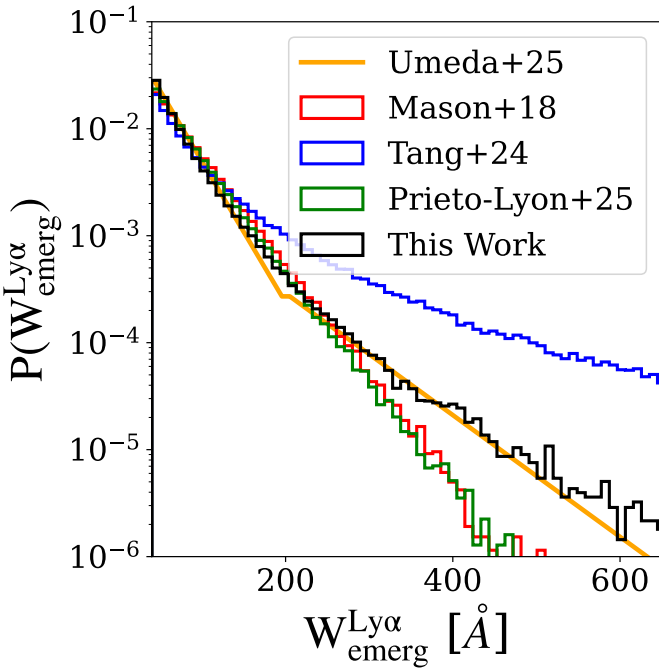


Fig. 6. The distribution of equivalent widths for $z \sim 5$ galaxies with $M_{\text{UV}} < -18$ reported by Umeda et al. (2025) (corresponding to a double power law fit to the data) is shown with the yellow curve. The corresponding marginal PDF predicted by our model is shown with the black histogram. The agreement of the yellow curves and the black histogram is an important sanity check for our model, as it was calibrated to independent data, with very different observational selections. For comparison, we also show the EW PDFs predicted by Mason et al. (2018), Tang et al. (2024a), and Prieto-Lyon et al. (2025). Our model matches the high EW tail of the PDF observed by Subaru better than previous estimates.

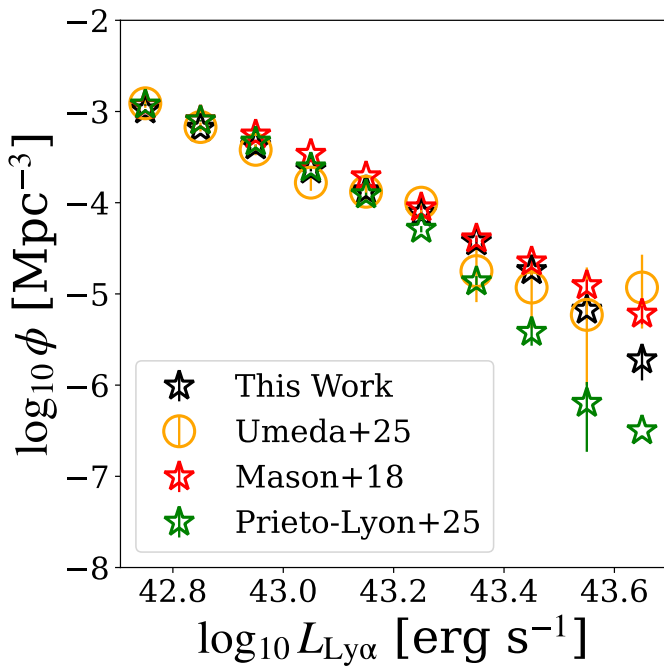


Fig. 7. The $z \sim 5$ Ly α luminosity function measured by Umeda et al. (2025) and predicted by the models of Mason et al. (2018), Prieto-Lyon et al. (2025), and this work.

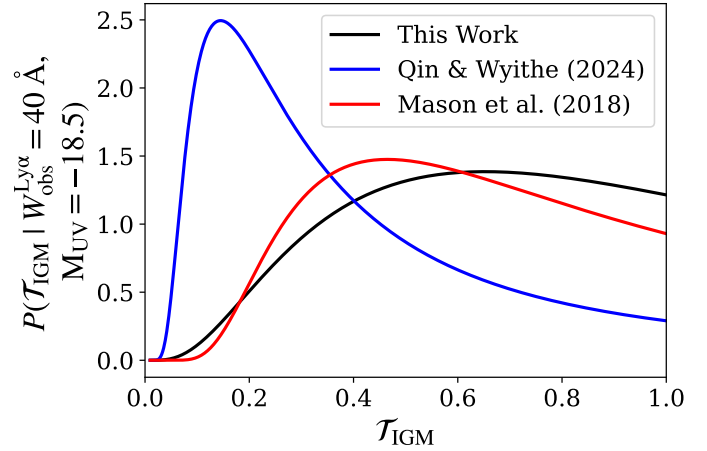


Fig. 8. Probability density functions of the IGM transmission fraction, \mathcal{T}_{IGM} in our model (black) and those of M18 (red) and Qin & Wyithe 2025 (blue), conditioned on having an observed Ly α equivalent width of 40 \AA , an emergent Ly α equivalent width larger than 40 \AA , and $M_{\text{UV}} = -18.5$, consistent with the properties of GS-z13 (Witstok et al. 2025).

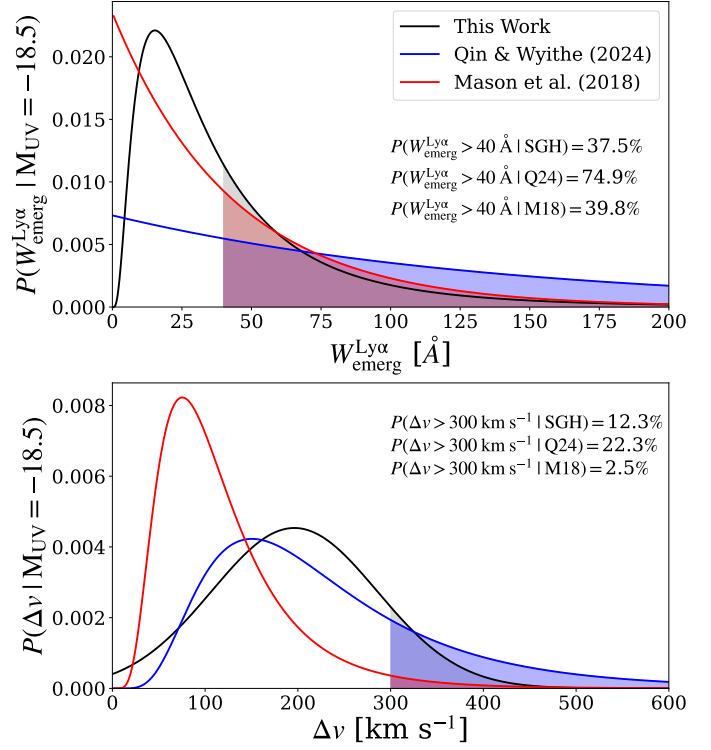


Fig. 9. The distributions of emergent Ly α equivalent widths (top) and red wing velocity offsets (bottom) for galaxies with $M_{\text{UV}} = -18.5$ in the empirical model presented in this work (black), as well as those presented by Mason et al. (2018) (blue) and Qin & Wyithe (2025) (red). The figure also lists the cumulative probabilities of $W_{\text{emerg}}^{\text{Ly}\alpha} > 40 \text{ \AA}$ (top) and $\Delta v > 300 \text{ km s}^{-1}$ (bottom) in each model.

Table 3. Observed properties of GS-z13.

Property	Units	Value
M_{UV}	-	-18.5
$W_{\text{obs}}^{\text{Ly}\alpha}$	\AA	40.0 ± 13.8
Ly α flux	$10^{-19} \text{ erg s}^{-1} \text{ cm}^{-2}$	7.46 ± 1.16
H β flux	$10^{-19} \text{ erg s}^{-1} \text{ cm}^{-2}$	< 6.7

Δv , see Dijkstra et al. 2011), and/or that it is sitting in an ionized bubble large enough to allow for significant Ly α transmission.

Given these uncertainties, the *observed* equivalent width of 40 Å can be treated as a lower limit to the *emergent* equivalent width. The two quantities are related by a factor that encodes the wavelength-averaged transmission through the patchy EoR:

$$\mathcal{T}_{\text{IGM}} = \frac{W_{\text{obs}}^{\text{Ly}\alpha}}{W_{\text{emerg}}^{\text{Ly}\alpha}}, \quad (19)$$

where \mathcal{T}_{IGM} is close to unity post EoR (as is assumed in our model calibrated at $z \sim 5$), and ranges to zero depending on the EoR stage and local morphology around the galaxy (e.g. Mesinger & Furlanetto 2008; Lu et al. 2024). Evaluating Eqs. 18 at GS-z13’s UV magnitude, $M_{\text{UV}} = -18.5$, we obtain $W_{\text{emerg}}^{\text{Ly}\alpha} = 30.49^{+39.36}_{-17.18}$ Å and $\Delta v = 197.19 \pm 89.17$ km s $^{-1}$, placing the object’s observed equivalent width within 1σ of the mean of our model’s distribution for the emergent equivalent width. From Eq. 19, we obtain that the implied IGM transmission is $\mathcal{T}_{\text{IGM}} = 0.62^{+0.25}_{-0.26}$, where the upper and lower bounds represent 16th and 84th percentiles. Figure 8 shows $P(\mathcal{T}_{\text{IGM}} | W_{\text{obs}}^{\text{Ly}\alpha} = 40 \text{ \AA}, W_{\text{emerg}}^{\text{Ly}\alpha} > 40 \text{ \AA}, M_{\text{UV}} = -18.5)$ for our model as well as those of M18 and Qin & Wyithe 2025, who recalibrated the M18 relations to better match the properties of recently detected Ly α -emitting galaxies from $2 < z < 11$ (Tang et al. 2024a; Witstok et al. 2024).

As discussed above, interpreting this value of the wavelength-averaged IGM transmission requires making assumptions about the local EoR morphology as well as the intrinsic velocity offset of the emergent Lyman alpha line. We defer a detailed study to future work; however, we note that Mason & Gronke (2020) estimated a minimum value of $\Delta v > 300$ km s $^{-1}$ would be required to detect Lyman alpha at those redshifts/EoR stages. Referring to Eq. 15, this minimum inferred value is only $\sim 1.1\sigma$ away from the mean of our distribution.

To put these in better context with previous studies, in Figure 9 we show our distributions of $W_{\text{emerg}}^{\text{Ly}\alpha}$ and Δv , evaluated at $M_{\text{UV}} = -18.5$ (black curves). We also show the corresponding PDFs for the empirical models of M18 (red curves) and Qin & Wyithe (2025) (blue curves). We highlight the probability densities beyond 40 Å and 300 km s $^{-1}$, expected to correspond to the emergent values of GS-z13 as discussed above. All three models can accommodate the lower limit of $W_{\text{emerg}}^{\text{Ly}\alpha} \approx 40$ Å with reasonable probabilities. However, the relatively high value of Δv derived by Mason & Gronke (2020) is considerably more likely in our model of the emergent profile and that of Qin & Wyithe (2025), compared to the M18 model.

As our model describes Ly α properties with a multivariate normal distribution with a non-diagonal covariance, it also quantifies the probability of galaxies having a certain Ly α property conditioned on its other Ly α properties. For example, given a known Ly α equivalent width and M_{UV} , we may produce the conditional distribution of velocity offsets, $P(\Delta v | W_{\text{emerg}}^{\text{Ly}\alpha}, M_{\text{UV}})$. In our model, the Δv is inversely correlated with $W_{\text{emerg}}^{\text{Ly}\alpha}$, bringing $P(W_{\text{emerg}}^{\text{Ly}\alpha} > 40 \text{ \AA})$ down to $\sim 13\%$ for $\Delta v = 300$ km s $^{-1}$, and lower beyond that. The formulas we employed to produce conditional distributions of our model are provided in Appendix H.

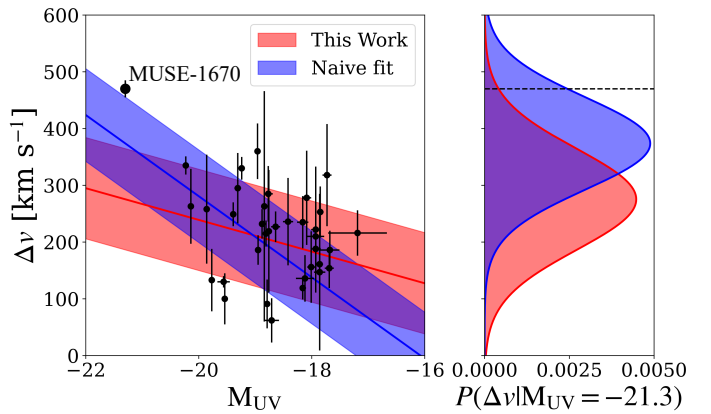


Fig. 10. The distribution of T24-Deep Ly α emitting galaxies in Δv and M_{UV} (black), with the size of the outlier MUSE-1670 exaggerated for emphasis. The mean value of $\Delta v(M_{\text{UV}})$ predicted by our model, with 1σ bounds, is overlaid in red. A naive relation obtained by linear regression is also overlaid in blue. The right panel shows the probability density functions of our model and the naive model at $M_{\text{UV}} = -21.3$, the M_{UV} of MUSE-1670. Our model clearly indicates that this object is an outlier, while the naive model does not.

4.3. Outlier detection: a GN-z11 analog at $z \approx 5$?

While most galaxies in the T24 sample lie well within the 95% probability density region predicted by our model (see Figure 5), we note one significant outlier: MUSE-1670 (located in the MUSE-Deep field, the galaxy with the highest Δv in the top middle panel of Figure 5).

The identification of outliers in a dataset depends on the assumed distribution of the data, which can vary greatly depending on how observational effects are accounted for. We illustrate this using a scatterplot of Δv and M_{UV} values of galaxies in the T24-Deep dataset in Figure 10. In red we overlay the $\Delta v - M_{\text{UV}}$ found by our model with 1σ scatter (c.f. Eq. 15) and in blue we overlay a linear regression to the data whose scatter is equal to the root mean squared difference between the data and the regression. The right panel shows the conditional probability distributions $P(\Delta v|M_{\text{UV}} = -21.3)$ for each model with the MUSE-1670 value indicated with the dashed line. Our model assigns a much lower probability density to the value of Δv measured for MUSE-1670, than the linear regression model. As such, our model allows us to accurately flag MUSE-1670 as an outlier, which would have otherwise been missed using the linear regression model.

In investigating this anomalous object, we noted a cursory similarity between its Ly α emission properties and those of the LAE GN-z11 (Bunker et al. 2023). These properties, as well as the conditional probability distributions for $P(W_{\text{emerg}}^{\text{Ly}\alpha}, \Delta v, f_{\text{esc}}^{\text{Ly}\alpha} | M_{\text{UV}} = -21.5)$ predicted by our model, are listed in Table 4. The escape fraction listed for our model assumes case A recombination: the value assuming case B recombination is 3% lower.

While both MUSE-1670 and GN-z11 have $f_{\text{esc}}^{\text{Ly}\alpha}$ and $W_{\text{emerg}}^{\text{Ly}\alpha}$ typical of $M_{\text{UV}} = -21.5$ galaxies, their Δv lie 2.12σ and 3.01σ above the modal value of our model, respectively. MUSE-1670 does not appear in any radio galaxy or active galactic nuclei (AGN) catalogs, nor does it feature broad line emission, meaning it is unlikely to be an anomalous AGN which survived the AGN exclusion selection of MUSE-Deep (Bacon et al. 2017). The JADES survey in the GOODS-S field targeted this galaxy with three separate pointings over the surface area of MUSE-

Table 4. The properties of GN-z11 (Bunker et al. 2023) and MUSE-1670 (Tang et al. 2024a) compared with the mean values of the conditional distribution $P(W_{\text{emerg}}^{\text{Ly}\alpha}, \Delta v, f_{\text{esc}}^{\text{Ly}\alpha} | M_{\text{UV}} = -21.5)$ predicted by our model, with 1σ bounds.

ID	M_{UV}	$W_{\text{emerg}}^{\text{Ly}\alpha} [\text{\AA}]$	$\Delta v [\text{km s}^{-1}]$	$f_{\text{esc}}^{\text{Ly}\alpha}$
GN-z11	-21.5	18.0	555	0.03 ± 0.05
MUSE-1670	-21.3 ± 0.01	29.0 ± 1.0	470.0 ± 15.0	0.06 ± 0.01
<i>This Work</i>	-21.5	$13.49^{+17.41}_{-7.60}$	280.95 ± 89.17	$0.10^{+0.20}_{-0.07}$

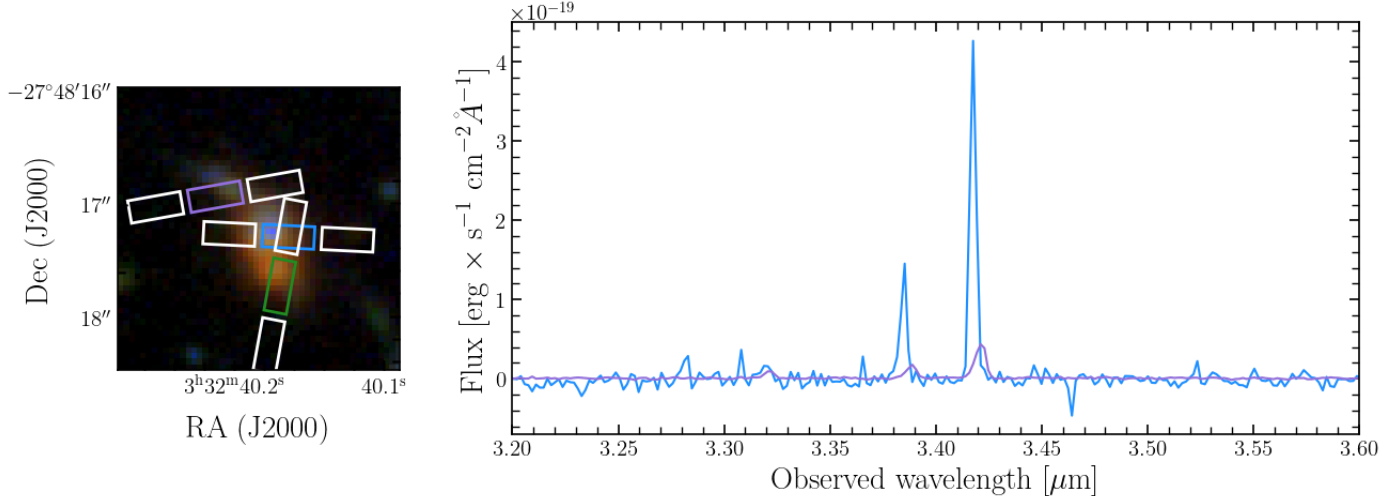


Fig. 11. The MUSE-1670 object with *JWST* pointings overlaid (left panel) and blue and purple spectra (right panel), taken from the JADES DR3 data release (D'Eugenio et al. 2025). The green spectrum is not included as it is not yet publicly available, but will be made so in the next JADES data release. The blue, purple, and green spectra all include $\text{H}\alpha$ at systemic redshifts of 5.8282, 5.8312, and 5.8193.

1670⁷, which is extended over ~ 5.9 proper kpc. Figure 11 shows MUSE-1670, along with the overlapping *JWST* pointings and measured spectra. The spectra yield slightly different systemic redshifts: 5.8282, 5.8312, and 5.8193 for the pointings colored purple, blue, and green in Figure 11, respectively. These correspond to velocity offsets of 2668 and 3573 km s^{-1} for the purple and blue spectra with respect to the rest frame of the green spectrum. The large spatial extent of MUSE-1670, different colors of its spatial components, and the vast range of systemic velocities support the interpretation that MUSE-1670 corresponds to a merging system. Interestingly, GN-z11 is similarly compact, with a proper size of 1.2 kpc (Bunker et al. 2023). If the $\text{Ly}\alpha$ properties of MUSE-1670 are typical of a merger-induced starburst, then we may posit that GN-z11 is also undergoing a merger.

4.4. Redshift evolution

Our model assumes that the probability distribution of emergent $\text{Ly}\alpha$ properties is conditional *only* on M_{UV} , and therefore its redshift evolution $dp(x_{\alpha})/dz$ is simply $dp(x_{\alpha})/dM_{\text{UV}} \times dM_{\text{UV}}/dz$. We expect this to be a reasonable approximation for $L_{\text{Ly}\alpha}$ and $L_{\text{H}\alpha}$, which both scale with the SFR that drives M_{UV} (e.g., Kennicutt 1998; Sobral & Matthee 2019), albeit with the caveat that $L_{\text{Ly}\alpha}$ and M_{UV} trace the SFR on 10 Myr and 100 Myr timescales, respectively, so any redshift evolution in the relationship between SFRs on these timescales (e.g., higher burstiness at earlier redshifts, c.f. Sun et al. 2025) could introduce shifts in our inferred relations at $z > 5 - 6$. Our approximation is unlikely to

hold as well for Δv , which is thought to more directly trace the gas mass (Stark et al. 2017; Hayes et al. 2023). Including explicit redshift dependence in $P(\Delta v)$ may increase the likelihood of observing objects like GS-z13 and GN-z11. In future work we will explore the physical causes of redshift evolution in $\text{Ly}\alpha$ observables and their impact on inferences of reionization.

5. Conclusion

We present a new empirical model of emergent $\text{Ly}\alpha$ emission intended for use in EoR studies. Our model is calibrated to the set of MUSE LAEs presented in Tang et al. (2024a) which also have detected $\text{H}\alpha$ from *JWST*. In our calibration, we forward-model the selection effects of both the MUSE and *JWST* surveys; this is crucial in avoiding spurious correlations induced by the selection. The resulting model is a conditional multivariate Gaussian described in Section 2.5. We list the defining characteristics of our model below.

- The distribution of $\log_{10} L_{\text{Ly}\alpha}$, Δv , and $\log_{10} L_{\text{H}\alpha}$ is a multivariate Gaussian whose mean varies with M_{UV} and whose covariance matrix is constant across M_{UV} .
- The inclusion of correlations between $\text{Ly}\alpha$ properties allows us to estimate conditional probabilities, such as $P(W_{\text{emerg}}^{\text{Ly}\alpha} | \Delta v)$, which is useful in cases where one property is measured while only a limit is available for another.
- The model calibration accounts for the expected number of LAEs in the survey area as a function of M_{UV} , enabling the model to reproduce the $\text{Ly}\alpha$ luminosity function without calibrating to additional data.
- Forward modeling of selection effects during calibration ensure that the covariances present in our model reflect the true distribution of the data.

⁷ MUSE-1670 may be viewed at this URL: <https://s3.amazonaws.com/grizli-v2/ClusterTiles/Map/gds/jwst.html?coord=53.1666918,-27.8042720&zoom=8>

Our model accurately reproduces the equivalent width probability density function and Ly α luminosity function of Umeda et al. (2025), even without additional calibration, as seen in Figures 6 and 7. It also predicts several scalings for Ly α parameters (Eq.s 14-17), reproducing the findings of Mason et al. (2018) and Prieto-Lyon et al. (2025) that low-UV luminosity galaxies tend to have higher $W_{\text{emerg}}^{\text{Ly}\alpha}$ and lower Δv . The principal physical implications of our model are listed below.

- Ly α equivalent width and escape fraction tend to increase with decreasing UV luminosity.
- The Ly α red wing velocity offset tends to increase with increasing UV luminosity.
- The only significant outlier in our calibration data, MUSE-1670, is likely undergoing a merger. This outlier incidentally has Ly α and galaxy characteristics similar to those of GN-z11, lending credence to the idea that GN-z11 may be a merger.
- Compared to some previous works, our model predicts a more extended distribution of equivalent widths and Ly α velocity offsets, which could facilitate the detection of Lyman alpha in the early EoR stages.
- We provide fitting functions in Eq.s 14-18 and make our code publicly available⁸.

Since our model has a clear separation of galaxy properties and survey parameters, one can include additional datasets with corresponding selection functions, thereby improving the inferred constraints on galaxy properties. With this new characterization of emergent Ly α from high- z galaxies, we will next try to robustly isolate EoR damping wing imprints from *JWST* and Subaru observations.

Acknowledgements. We thank M. Wyatt, C. Mason, D. Stark for insightful comments on a draft version of this work. We extend further gratitude to B. Trefoloni, S. Shanbhog, and S. Carniani for useful discussion on observational effects. We gratefully acknowledge computational resources of the HPC center at SNS. AM acknowledges support from the Italian Ministry of Universities and Research (MUR) through the PRIN project “Optimal inference from radio images of the epoch of reionization”, and the PNRR project “Centro Nazionale di Ricerca in High Performance Computing, Big Data e Quantum Computing”.

References

Bacon, R., Brinchmann, J., Conseil, S., et al. 2023, A&A, 670, A4

Bacon, R., Conseil, S., Mary, D., et al. 2017, A&A, 608, A1

Baker, J. G. & Menzel, D. H. 1938, ApJ, 88, 52

Barkana, R. & Loeb, A. 2003, Nature, 421, 341

Behrens, C., Byrohl, C., Saito, S., & Niemeyer, J. C. 2018, A&A, 614, A31

Behrens, C., Pallottini, A., Ferrara, A., Gallerani, S., & Vallini, L. 2019, MNRAS, 486, 2197

Bolan, P., Lemaux, B. C., Mason, C., et al. 2022, MNRAS, 517, 3263

Bouwens, R. J., Illingworth, G. D., Oesch, P. A., et al. 2014, The Astrophysical Journal, 793, 115

Bouwens, R. J., Oesch, P. A., Stefanon, M., et al. 2021, AJ, 162, 47

Bunker, A. J., Saxena, A., Cameron, A. J., et al. 2023, A&A, 677, A88

Byrohl, C. & Gronke, M. 2020, A&A, 642, L16

Chen, Z., Stark, D. P., Mason, C., et al. 2024, MNRAS, 528, 7052

Chirkjian, G. S. 2011, Stochastic Models, Information Theory, and Lie Groups, Volume 2: Analytic Methods and Modern Applications, 1st edn. (Boston, MA: Birkhäuser)

Davies, J. E., Mesinger, A., & Murray, S. 2025, submitted to A&A, in review, arXiv:2504.17254

Dayal, P. & Ferrara, A. 2018, Phys. Rep., 780, 1

De Barros, S., Pentericci, L., Vanzella, E., et al. 2017, A&A, 608, A123

D’Eugenio, F., Cameron, A. J., Scholtz, J., et al. 2025, ApJS, 277, 4

Di Cesare, C., Matthee, J., Naidu, R. P., et al. 2025, arXiv e-prints, arXiv:2510.19044

Dijkstra, M. 2014, PASA, 31, e040

Dijkstra, M., Mesinger, A., & Wyithe, J. S. B. 2011, MNRAS, 414, 2139

Dijkstra, M. & Wyithe, J. S. B. 2012, MNRAS, 419, 3181

Eisenstein, D. J., Willott, C., Alberts, S., et al. 2023, arXiv e-prints, arXiv:2306.02465

Fardal, M. A., Katz, N., Gardner, J. P., et al. 2001, ApJ, 562, 605

Fletcher, P., Lu, C., & Joshi, S. 2003, in 2003 IEEE Computer Society Conference on Computer Vision and Pattern Recognition, 2003. Proceedings., Vol. 1, I-I

Furlanetto, S. R., Oh, S. P., & Briggs, F. H. 2006, Phys. Rep., 433, 181

Gagnon-Hartman, S., Davies, J. E., & Mesinger, A. 2025, A&A, 699, A131

Gelli, V., Mason, C., Pallottini, A., et al. 2025, arXiv e-prints, arXiv:2510.01315

Gnedin, N. Y. & Hui, L. 1998, MNRAS, 296, 44

Greif, T. H., Johnson, J. L., Klessen, R. S., & Bromm, V. 2009, MNRAS, 399, 639

Gronke, M. 2017, A&A, 608, A139

Gronke, M., Dijkstra, M., McCourt, M., & Oh, S. P. 2016, ApJ, 833, L26

Gurung-López, S., Byrohl, C., Gronke, M., et al. 2025, A&A, 698, A139

Haiman, Z., Spaans, M., & Quataert, E. 2000, ApJ, 537, L5

Hayes, M., Östlin, G., Schaerer, D., et al. 2010, Nature, 464, 562

Hayes, M. J., Runnholm, A., Scarlata, C., Gronke, M., & Rivera-Thorsen, T. E. 2023, MNRAS, 520, 5903

Hutter, A., Dayal, P., Müller, V., & Trott, C. M. 2017, ApJ, 836, 176

Jones, G. C., Bunker, A. J., Saxena, A., et al. 2025, MNRAS, 536, 2355

Jung, I., Finkelstein, S. L., Dickinson, M., et al. 2020, ApJ, 904, 144

Kennicutt, Robert C., J. 1998, ARA&A, 36, 189

Khoramnezhad, H., Saito, S., Gronke, M., & Byrohl, C. 2025, arXiv e-prints, arXiv:2507.16707

Li, Z. & Gronke, M. 2022, MNRAS, 513, 5034

Lu, T.-Y., Mason, C. A., Mesinger, A., et al. 2024, arXiv e-prints, arXiv:2411.04176

Lu, T.-Y., Mason, C. A., Mesinger, A., et al. 2025, A&A, 697, A69

Mason, C. A. & Gronke, M. 2020, MNRAS, 499, 1395

Mason, C. A., Treu, T., Dijkstra, M., et al. 2018, ApJ, 856, 2

Mason, C. A., Treu, T., Schmidt, K. B., et al. 2015, ApJ, 805, 79

Matthee, J., Sobral, D., Oteo, I., et al. 2016, MNRAS, 458, 449

McQuinn, M., Lidz, A., Zahn, O., et al. 2007, MNRAS, 377, 1043

Mesinger, A., ed. 2016, Astrophysics and Space Science Library, Vol. 423, Understanding the Epoch of Cosmic Reionization

Mesinger, A., Aykutalp, A., Vanzella, E., et al. 2015, MNRAS, 446, 566

Mesinger, A. & Furlanetto, S. R. 2008, MNRAS, 385, 1348

Mirocha, J., Furlanetto, S. R., & Sun, G. 2017, MNRAS, 464, 1365

Morales, A. M., Mason, C. A., Bruton, S., et al. 2021, ApJ, 919, 120

Nakane, M., Ouchi, M., Nakajima, K., et al. 2024, ApJ, 967, 28

Napolitano, L., Pentericci, L., Dickinson, M., et al. 2025, arXiv e-prints, arXiv:2508.14171

Napolitano, L., Pentericci, L., Santini, P., et al. 2024, A&A, 688, A106

Nebrin, O., Smith, A., Lorinc, K., et al. 2025, MNRAS, 537, 1646

Neufeld, D. A. 1990, ApJ, 350, 216

Nikolić, I., Mesinger, A., Greig, B., & Gillet, N. 2024, MNRAS, 484, 933

Nikolić, I., Mesinger, A., Mason, C. A., et al. 2025, arXiv e-prints, arXiv:2501.07980

Oesch, P. A., Brammer, G., Naidu, R. P., et al. 2023, MNRAS, 525, 2864

Osterbrock, D. E. 1989, Astrophysics of gaseous nebulae and active galactic nuclei

Park, J., Mesinger, A., Greig, B., & Gillet, N. 2019, MNRAS, 484, 933

Pawlak, A. H., Milosavljević, M., & Bromm, V. 2011, ApJ, 731, 54

Pentericci, L., McLure, R. J., Garilli, B., et al. 2018, A&A, 616, A174

Planck Collaboration, Aghanim, N., Akrami, Y., et al. 2020, A&A, 641, A6

Prieto-Lyon, G., Mason, C. A., Strait, V., et al. 2025, arXiv e-prints, arXiv:2509.18302

Qin, Y., Mesinger, A., Prelogović, D., et al. 2024, submitted to PASA, in review, arXiv:2412.00799

Qin, Y. & Wyithe, J. S. B. 2025, MNRAS, 538, L16

Raiter, A., Schaerer, D., & Fosbury, R. A. E. 2010, A&A, 523, A64

Saxena, A., Bunker, A. J., Jones, G. C., et al. 2024, A&A, 684, A84

Saxena, A., Robertson, B. E., Bunker, A. J., et al. 2023, A&A, 678, A68

Schenker, M. A., Ellis, R. S., Konidaris, N. P., & Stark, D. P. 2014, ApJ, 795, 20

Smith, A., Kannan, R., Garaldi, E., et al. 2022, MNRAS, 512, 3243

Smith, A., Lorinc, K., Nebrin, O., & Lao, B.-X. 2025, MNRAS, 541, 179

Sobacchi, E. & Mesinger, A. 2015, MNRAS, 453, 1843

Sobral, D. & Matthee, J. 2019, A&A, 623, A157

Stark, D. P., Ellis, R. S., Charlton, S., et al. 2017, MNRAS, 464, 469

Stark, D. P., Ellis, R. S., Chiu, K., Ouchi, M., & Bunker, A. 2010, MNRAS, 408, 1628

Storn, R. & Price, K. 1997, Journal of Global Optimization, 11, 341

Sun, G. & Furlanetto, S. R. 2016, MNRAS, 460, 417

Sun, G., Muñoz, J. B., Mirocha, J., & Faucher-Giguère, C.-A. 2025, J. Cosmology Astropart. Phys., 2025, 034

Tang, M., Stark, D. P., Chen, Z., et al. 2023, MNRAS, 526, 1657

Tang, M., Stark, D. P., Ellis, R. S., et al. 2024a, MNRAS, 531, 2701

Tang, M., Stark, D. P., Topping, M. W., Mason, C., & Ellis, R. S. 2024b, ApJ, 975, 208

Treu, T., Trenti, M., Stiavelli, M., Auger, M. W., & Bradley, L. D. 2012, ApJ, 747, 27

Trotta, R. 2008, Contemporary Physics, 49, 71

Umeda, H., Ouchi, M., Kikuta, S., et al. 2025, ApJS, 277, 37

Umeda, H., Ouchi, M., Nakajima, K., et al. 2024, ApJ, 971, 124

Urrutia, T., Wisotzki, L., Kerutt, J., et al. 2019, A&A, 624, A141

Verhamme, A., Dubois, Y., Blaizot, J., et al. 2012, A&A, 546, A111

Vitte, E., Verhamme, A., Hibon, P., et al. 2025, A&A, 694, A100

Witstok, J., Maiolino, R., Smit, R., et al. 2025, MNRAS, 536, 27

Witstok, J., Smit, R., Saxena, A., et al. 2024, A&A, 682, A40

Yang, H., Malhotra, S., Gronke, M., et al. 2017, ApJ, 844, 171

⁸ https://github.com/samgagnon/empirical_lya

Appendix A: SO(3) Lie group

The basis space of the change of basis matrix A spans the space of all 3D rotations plus the space of all scalar multiples via the identity matrix (Fletcher et al. 2003). While the full set of 3D basis transformations also includes stretching and shearing, the matrix A operates on a quantity which is already normalized to have unit variance, and should therefore not be related to its orthonormal basis by a stretch transformation. Furthermore, our basis can still produce the subset of shear transformations which lie in the convex cone generated by \mathcal{I} and SO(3) (Chirikjian 2011). While this does not cover all possible shear transformations, we assume that it contains at a minimum one of the shear transformations required to orthonormalize the T24 data. Since our MLE converged on a convincing solution, we deem these assumptions reasonable.

The transformation matrices of the SO(3) Lie group are

$$S_1 = \begin{bmatrix} 0 & 0 & 0 \\ 0 & 0 & -1 \\ 0 & 1 & 0 \end{bmatrix}, S_2 = \begin{bmatrix} 0 & 0 & 1 \\ 0 & 0 & 0 \\ -1 & 0 & 0 \end{bmatrix}, \text{ and } S_3 = \begin{bmatrix} 0 & -1 & 0 \\ 1 & 0 & 0 \\ 0 & 0 & 0 \end{bmatrix}. \quad (\text{A.1})$$

Linear combinations of SO(3) rotation matrices are themselves also rotation matrices, therefore preserving the origin about which vectors are rotated and the magnitude of the vector. By defining our change of basis matrix A as a linear combination of SO(3) rotation group matrices and the identity matrix, we impose that the data vector x_α is a linear combination of u with a 3D rotation of u .

Appendix B: Gaussian likelihood function

In the second step of our model calibration procedure, we minimize the objective function

$$\text{obj} = \sum^i \sum_j \left(\frac{\langle y \rangle_j^i - \mu_j^i}{\sigma_j^i} \right)^2, \quad (\text{B.1})$$

where i represents the index of each dataset, j represents the index of each quantity computed from our model and the data, $\langle y \rangle_j^i$ is the expectation value of quantity j assuming the selection function of i computed from our model, μ_j^i is the same quantity computed from the data, and σ_j^i is the standard deviation of that quantity in the data. We use

$$i \in \{\text{T24 - Wide, T24 - Deep}\}, j \in \{f_{\text{obs}}(M_{\text{UV}}), W_{\text{emerg}}^{\text{Ly}\alpha}(M_{\text{UV}}), \Delta v(M_{\text{UV}}), f_{\text{esc}}^{\text{Ly}\alpha}(M_{\text{UV}})\}, \quad (\text{B.2})$$

where each quantity in j is computed for 20 equal bins in M_{UV} ranging from -20 to -17 .

Appendix C: Model parameters

Table C.1 lists all parameters of our model.

Appendix D: Multivariate normal parameterization of model

The model of $P(\log_{10} L_{\text{Ly}\alpha}, \Delta v, \log_{10} L_{\text{H}\alpha} | M_{\text{UV}})$ presented in this work may be written in closed form as a multivariate normal distribution

$$\begin{bmatrix} \log_{10} L_{\text{Ly}\alpha} \\ \Delta v \\ \log_{10} L_{\text{H}\alpha} \end{bmatrix} = \mathcal{N} \left(\begin{bmatrix} -0.28(M_{\text{UV}} + 18.5) + 41.86 \text{ erg s}^{-1} \text{ cm}^{-2} \\ -27.92(M_{\text{UV}} + 18.5) + 197.19 \text{ km s}^{-1} \\ -0.38(M_{\text{UV}} + 18.5) + 41.64 \text{ erg s}^{-1} \text{ cm}^{-2} \end{bmatrix}, \begin{bmatrix} 0.13 & -0.11 & 0.02 \\ -0.11 & 7998.70 & 13.26 \\ 0.02 & 13.26 & 0.06 \end{bmatrix} \right), \quad (\text{D.1})$$

where the entries of \mathcal{N} are its mean, μ , and covariance, Σ .

Appendix E: Equivalent width PDF

Figure E.1 shows the distribution of Ly α equivalent widths (EWPDF) for galaxies at $z \sim 5$ with $M_{\text{UV}} \leq -18$ measured by Umeda et al. (2025) and predicted by the models of Mason et al. (2018) (M18) and this work. We posit that our model can better reproduce the measured EWPDF because it is calibrated on both a deep (long exposure, small angular area) and a wide (short exposure, large angular area) dataset. The former should be dominated by dimmer, more numerous objects, while the latter should be brighter, rarer objects. These correspond to the peak and faint tail of the EWPDF, respectively.

To investigate this hypothesis, we recalibrated our model using only the T24-Deep dataset, and then again using only the T24-Wide dataset (see Table 2). The EWPDFs arising from these models are shown in dashed and dotted curves in Figure E.1. The bottom panel includes the residuals of each model with respect to the measured EWPDF of Umeda et al. (2025). Note that while

Table C.1. All model parameters, including the selection criteria with prior ranges.

Parameter	Description	Prior range	Optimal value
c_1	transformation coefficient 1	$[-1, 1]$	1.0
c_2	transformation coefficient 2	$[-1, 1]$	1.0
c_3	transformation coefficient 3	$[-1, 1]$	0.34
c_4	transformation coefficient 4	$[-1, 1]$	-1.0
m_1	slope of mean of eigenvector 1	$[-1, 1]$	$8.7 \cdot 10^{-2}$
m_2	slope of mean of eigenvector 2	$[-1, 1]$	-0.57
m_3	slope of mean of eigenvector 3	$[-1, 1]$	-0.38
b_1	intercept of mean of eigenvector 1	$[-3, 3]$	-0.51
b_2	intercept of mean of eigenvector 2	$[-3, 3]$	-0.85
b_3	intercept of mean of eigenvector 3	$[-3, 3]$	-0.31
σ_1	standard deviation of eigenvector 1	$[0.01, 1.0]$	0.70
σ_2	standard deviation of eigenvector 2	$[0.01, 1.0]$	0.49
σ_3	standard deviation of eigenvector 3	$[0.01, 1.0]$	0.26
W_{Wide}	MUSE-Wide Ly α EW limit	$[40, 120]$	116
W_{Deep}	MUSE-Deep Ly α EW limit	$[12.5, 50]$	24
f_{Wide}	MUSE-Wide Ly α flux limit	$[10^{-17}, 3 \cdot 10^{-17}]$	$1.8 \cdot 10^{-17}$
f_{Deep}	MUSE-Deep Ly α flux limit	$[10^{-18}, 3 \cdot 10^{-18}]$	$2.7 \cdot 10^{-18}$
f_{JWST}	<i>JWST</i> H α flux limit	$[10^{-18}, 3 \cdot 10^{-18}]$	$1.2 \cdot 10^{-18}$
$\mu_{\text{Ly}\alpha}$	mean of data in MUSE-Deep field	-	{42.47, 200.18, 42.03}
$\sigma_{\text{Ly}\alpha}$	standard deviation of data in MUSE-Deep field	-	{0.42, 99.7, 0.39}

the Deep-only model diverges significantly from all other models at high equivalent widths, it converges to the M18 model at low equivalent widths. This makes sense since the calibration sample of the M18 model were rare faint objects similar to those in the T24-Deep sample. Meanwhile, the Wide-only model more accurately fits the measured relation up to an equivalent width of ~ 200 , but then diverges. The measured relation is only convincingly recovered when both datasets are included.

It is possible that the variance in the $M_{\text{UV}} - W_{\text{emerg}}^{\text{Ly}\alpha}$ relation dominates the probability density at the faint end of the EWPDF. In this case, the model calibrated to both datasets is better able to recover that faint end thanks to its accurate determination of the variance in the $M_{\text{UV}} - W_{\text{emerg}}^{\text{Ly}\alpha}$ relation, constrained by fitting the observed fractions shown in Figure 3.

Appendix F: M18 recalibration

The recalibrated M18-like relations for the probability of emitting Ly α with $f_{\text{Ly}\alpha} \geq 2 \cdot 10^{-18} \text{ erg s}^{-1}$ is $A(M_{\text{UV}})$ and the mean equivalent width is $W_c(M_{\text{UV}})$ are:

$$A(M_{\text{UV}}) = 0.50 - 0.50 \tanh [0.67(M_{\text{UV}} + 18.0)], \quad (\text{F.1})$$

and

$$W_c(M_{\text{UV}}) = 13.95 + 169.09 \exp [0.64(M_{\text{UV}} + 16.5)] \text{ \AA}. \quad (\text{F.2})$$

Our model assumes that all galaxies emit in Ly α . For the purposes of recalibrating the M18 model, we compute $A(M_{\text{UV}})$ as the fraction of emitters with $f_{\text{Ly}\alpha} \geq 2 \cdot 10^{-18} \text{ erg s}^{-1}$, as this was the 5σ detection threshold of the VANDELS survey (Pentericci et al. 2018). The tanh function reported for $A(M_{\text{UV}})$ in Eq. F.1 fits our model extremely well. This makes sense since we model $P(\log_{10} L_{\text{Ly}\alpha} | M_{\text{UV}})$ as a Gaussian distribution, whose cumulative distribution function, the error function, is very similar in form to the tanh function. We fit $W_c(M_{\text{UV}})$ to the mean equivalent width assuming $f_{\text{Ly}\alpha} \geq 2 \cdot 10^{-18}$, i.e. $\mathbb{E}\{P(W_{\text{Ly}\alpha} | M_{\text{UV}}, f_{\text{Ly}\alpha} \geq 2 \cdot 10^{-18})\}$. Here the tanh function is less appropriate. While the best-fit tanh holds well for $M_{\text{UV}} \approx 18$ and fainter, its error exceeds 5% at $M_{\text{UV}} = -21$ and reaches 30% at $M_{\text{UV}} = -22$. Switching to an exponential distribution reduces all errors in the range $M_{\text{UV}} \in [-22, -16]$ to $< 5\%$.

Appendix G: $M_h - M_{\text{UV}}$ relation

In our investigation of the $\Delta v - M_{\text{UV}}$ relation predicted by our model, we employed the $M_{\text{UV}} - M_h$ relation of Davies et al. (2025). In that work, M_{UV} is treated as a function of the star formation rate, following the implementation of Park et al. (2019):

$$M_{\text{UV}} = 51.6 - 2.5 \log_{10} \left(\frac{\text{SFR}}{\kappa_{\text{UV}}} \right), \quad (\text{G.1})$$

where $\kappa_{\text{UV}} = 1.15 \cdot 10^{-28} M_{\odot} \text{ yr}^{-1} \text{ erg}^{-1} \text{ s Hz}$, following Sun & Furlanetto (2016). Davies et al. (2025) samples SFR from the log-normal distribution:

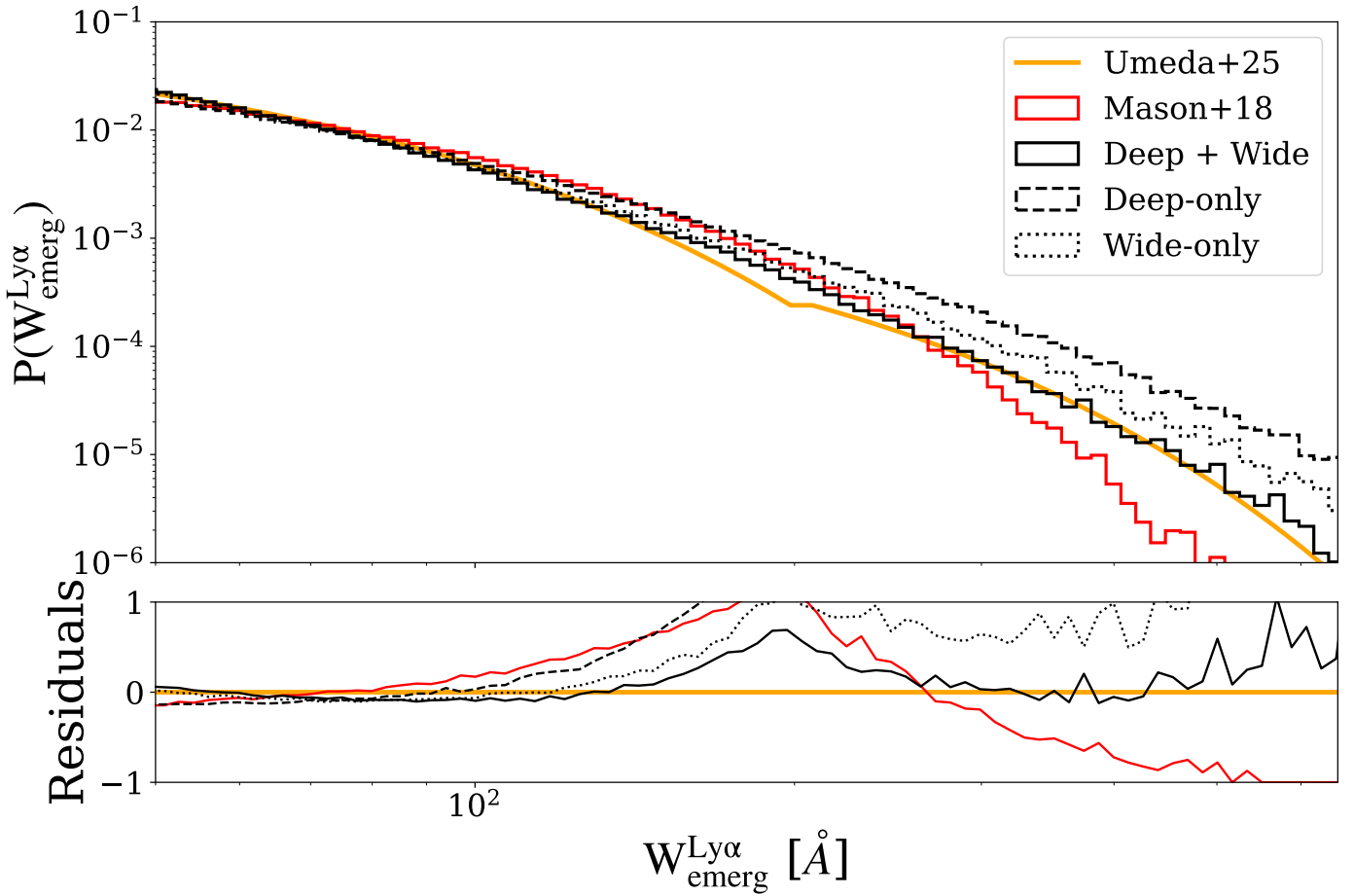


Fig. E.1. The distribution of equivalent widths for $z \sim 5$ galaxies with $M_{\text{UV}} \leq -18$ measured by Umeda et al. (2025) (orange) and predicted by the models of Mason et al. (2018) (red) and this work (black). The dashed and dotted curves show the fits which would be obtained if we used only the T24-Deep and T24-Wide datasets (see Table 2), respectively, in our model calibration. The bottom panel shows residuals against the measured relation.

$$P(\ln(\text{SFR})|M_*) = \mathcal{N}(\mu_{\text{SFR}}(M_*), \sigma_{\text{SFR}}(M_*)), \quad (\text{G.2})$$

where M_* is the stellar mass, and μ_{SFR} and σ_{SFR} are functions of M_* . The mean follows the relation

$$\mu_*(M_*) = \frac{M_*}{t_* H(z)} \quad (\text{G.3})$$

from Park et al. (2019), where $t_* = 0.5$ and $H(z)$ is the Hubble constant at redshift z . The standard deviation increases with increasing stellar mass according to a double power-law:

$$\sigma_{\text{SFR}} = \max \left(\sigma_{\text{SFR,lim}}, \sigma_{\text{SFR,} \text{idx}} \log_{10} \left(\frac{M_*}{10^{10} M_\odot} \right) + \sigma_{\text{SFR,lim}} \right), \quad (\text{G.4})$$

where $\sigma_{\text{SFR,lim}} = 0.19$ and $\sigma_{\text{SFR,} \text{idx}} = -0.12$. Similarly, Davies et al. (2025) sample M_* from the log-normal distribution

$$P(\ln M_*|M_h) = \mathcal{N}(\mu_*(M_h), \sigma_*), \quad (\text{G.5})$$

where $\sigma_* = 0.5$ and $\mu_*(M_h)$ is the scaling relation of Mirocha et al. (2017):

$$\mu_*(M_h) = f_{*,10} \left(\frac{(M_{\text{pivot}}/10^{10} M_\odot)^{\alpha_*} + (M_{\text{pivot}}/10^{10} M_\odot)^{\alpha_{*2}}}{(M_h/10^{10} M_\odot)^{-\alpha_*} + (M_h/10^{10} M_\odot)^{-\alpha_{*2}}} \right) M_h \exp \left(-\frac{M_{\text{turn}}}{M_h} \right) \frac{\Omega_b}{\Omega_m}, \quad (\text{G.6})$$

where $M_{\text{pivot}} = 2.8 \cdot 10^{11} M_\odot$, $\alpha_* = 0.5$, $\alpha_{*2} = -0.61$, and $M_{\text{turn}} = 5 \cdot 10^8 M_\odot$.

Using the equations above, we computed $P(M_{\text{UV}}|M_h)$ for $M_h \in [10^8 M_\odot, 10^{12} M_\odot]$ and inverted this distribution numerically to produce $P(M_h|M_{\text{UV}})$.

Appendix H: Conditional probabilities of the multivariate normal distribution

Let x follow a multivariate normal distribution $x \sim \mathcal{N}(\mu, \Sigma)$, characterized by its mean, μ , and covariance matrix Σ , with components

$$\mu = \begin{bmatrix} \mu_1 \\ \mu_2 \\ \mu_3 \end{bmatrix}, \quad (H.1)$$

and

$$\Sigma = \begin{bmatrix} \Sigma_{11} & \Sigma_{12} \\ \Sigma_{21} & \Sigma_{22} \end{bmatrix}. \quad (H.2)$$

The probability distribution of x_1 conditioned on a value of x_2 drawn from the same distribution is

$$P(x_1|x_2) = \mathcal{N}(\mu_{1|2}, \Sigma_{1|2}), \quad (H.3)$$

where

$$\mu_{1|2} = \mu_1 + \Sigma_{12}\Sigma_{22}^{-1}(x_2 - \mu_2) \quad (H.4)$$

and

$$\Sigma_{1|2} = \Sigma_1 - \Sigma_{12}\Sigma_{22}^{-1}\Sigma_{21}. \quad (H.5)$$

Using these expressions, we may obtain a closed form also for $P(x_1|x_2 > X_2)$, where X_2 is some fixed minimum value of x_2 . This is

$$P(x_1|x_2 > X_2) \propto P(x_1) \int_{X_2}^{\infty} P(x_2|x_1)dx_2, \quad (H.6)$$

which, using the cumulative density function of the normal distribution, $\Phi(X; \mu, \Sigma)$, is

$$P(x_1|x_2 > X_2) \propto P(x_1) [1 - \Phi(X_2; \mu_{2|1}, \Sigma_{2|1})]. \quad (H.7)$$

Similarly, the probability density function of x_1 given a maximum value of x_2 is

$$P(x_1|x_2 < X_2) \propto P(x_1)\Phi(X_2; \mu_{2|1}, \Sigma_{2|1}). \quad (H.8)$$